Pure Appl. Geophys.

https://doi.org/10.1007/s00024-024-03467-3

Pure and Applied Geophysics

Stratospheric Gravity Waves Impact on Infrasound Transmission Losses Across the International Monitoring System

C. Listowski,[1] C. C. Stephan,[2] A. Le Pichon,[1] A. Hauchecorne,[3] Y.-H. Kim,[4] U. Achatz,[5] and G. Bölöni[6]

Abstract—The international monitoring system (IMS) has been put in place to monitor compliance with the comprehensive nuclear-test-ban treaty (CTBT). Its infrasound component, dedicated to the monitoring of atmospheric events, gives also room to civil applications (e.g. monitoring of volcanic eruptions, meteorites, severe weather). Infrasound detection capabilities are largely determined by the state of the middle atmosphere. This requires an accurate knowledge of the atmospheric processes at play. More particularly internal gravity waves (GW) pose a challenge to atmospheric modelling because of unresolved processes. Using high-resolution simulation outputs over winter 2020 (20 January–1 March) we present a method to assess the impact of GW on infrasound surface transmission losses across the IMS. We validate the method by comparing simulated GW perturbations to GW lidar observations at Observatoire de Haute-Provence in France, and satellite-based GW energy estimations globally. We perform propagation simulations using atmospheric specifications where GW are filtered out and kept in, respectively. We demonstrate that the largest impact of GW across the IMS is not where GW activity is the largest, but rather where GW activity combines with infrasound waveguides not firmly set in a given direction. In northern winter, the largest variations of transmission losses at 1 Hz due to GW occur in the southern (summer) hemisphere in the direction of the main guide (westward propagation), with average values ranging between 10 and 25 dB in the first shadow zone. It corresponds to an average signal amplification of at least a factor 5 to 15, while this amplification is around 2 to 5 for the main guide in the northern winter hemisphere (eastward propagation).

Keywords: Infrasound, Middle atmospheric dynamics, Gravity waves, Stratosphere, Atmospheric model, ICON.

1. Introduction

The infrasound component of the international monitoring system (IMS) is one of the four verification technologies for the comprehensive nuclear-test-ban treaty (CTBT). Its detection capability is primarily modulated by middle atmospheric winds and temperatures (Le Pichon et al., 2012, 2019). Infrasound guiding across large distances (hundreds to thousands of kilometers) is made possible because of the low frequency of these acoustic waves (typically 0.003–20 Hz) compared to audible sound (above 20 Hz). The average distance between two IMS infrasound stations is $\sim$ 2000 km (Fig. 1), making a given acoustic source less than $\sim$ 1000 km away from the nearest IMS station on average, provided propagation conditions are met. The nominal frequency range of interest to the IMS is defined as 0.02–4 Hz (e.g. Brachet et al., 2010), which is adapted to the main frequencies generated by explosions at regional to synoptic scales (e.g. Ceranna et al., 2009; Pilger et al., 2021). Aside from artificial sources like explosions, acoustic monitoring of the atmosphere allows to investigate, locate, and, or, track geophysical events like volcanic eruptions (e.g. Marchetti et al., 2019), meteorite entries (e.g. Pilger et al., 2020), and cyclones (e.g. Listowski et al., 2022). This demonstrates possible civil applications of the IMS network and bring novel datasets for investigating fundamental processes involved in these natural acoustic sources, from regional scales (a few hundreds of km) to synoptic and global scales (thousand km and more).

The efficiency of atmospheric waveguides is essentially determined by the seasonal changes of winds in the stratosphere, while the thermospheric

[1] CEA, DAM, DIF, 91297 Arpajon, France. E-mail: constantino.listowski@cea.fr
[2] Leibniz Institute of Atmospheric Physics at the University of Rostock, Kühlungsborn, Germany.
[3] LATMOS/IPSL, UVSQ Université Paris-Saclay, Sorbonne Université, CNRS, Guyancourt, France.
[4] Seoul National University, Seoul, South Korea.
[5] Goethe-Universität Frankfurt, Frankfurt, Germany.
[6] Deutscher Wetterdienst, Offenbach am Main, Germany.

Published online: 13 April 2024

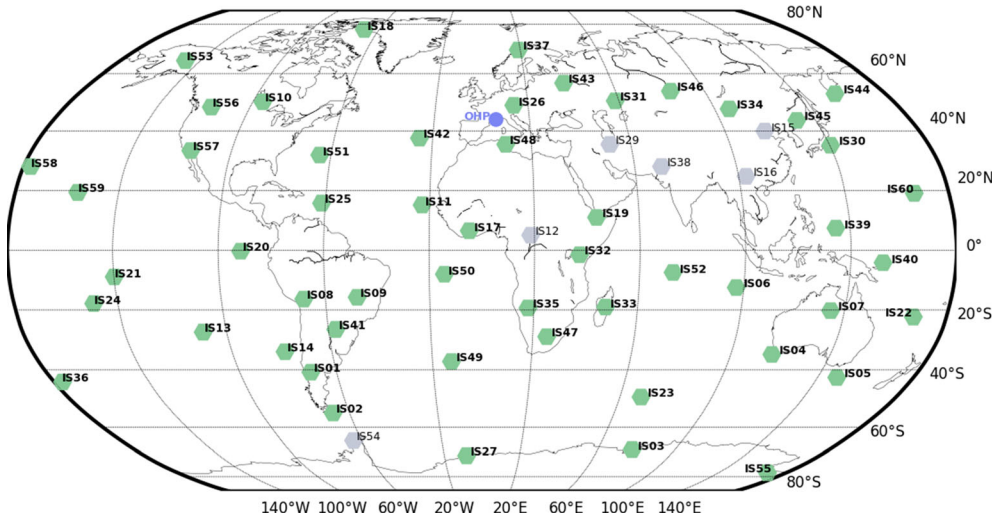

Figure 1
The infrasound component of the international monitoring system (IMS) with operational stations shown in green and planned stations in grey, as of today. The Observatoire de Haute-Provence (OHP) where lidar temperature observations used in this work are routinely made is shown with a blue filled circle

guide exists in any direction because of the positive temperature gradient in the mesosphere-lower thermosphere (MLT) (Drob et al., 2003). Stratospheric winds are driven by the meridional temperature gradient between polar and lower latitude regions in virtue of geostrophic balance and thermal wind balance. Westerly winds are dominant in the winter season and easterly winds in the summer season in the mid-latitudes of both hemispheres. In equatorial regions, the Semi-Annual Oscillation shapes annual detection patterns as demonstrated by systematic lightning detections across 15 years at a tropical station (Farges et al., 2021). The enhanced absorption of waves along thermospheric paths for higher and higher frequencies results in stronger attenuation of the signals compared with stratospheric phases (Sutherland & Bass, 2004). This explains the prevalence of stratospheric returns in routinely monitored signals. However, source characterization can significantly benefit from the careful examination of exclusive thermospheric paths (Blom and Waxler, 2021). For stratospheric phases, reference meteorological products routinely used by National Data Centers can fail predicting detections or lack detections at regional scales because of inaccuracies in the simulated fields (Pilger et al., 2023). This calls for more investigations on the processes affecting the IMS network detection capabilities.

Atmospheric internal gravity waves (GW) are critical to guiding conditions as they alter the propagation path of infrasound waves by perturbing the wind and temperature fields. They cause detections at infrasound stations that remain unexplained when only large-scale atmospheric features are considered (e.g. Drob et al., 2013; Hedlin & Drob, 2014). GW can significantly affect IMS detection capability maps globally (Le Pichon et al., 2019). This holds particularly true during the equinoxes where mid-latitude stratospheric winds are transitioning from one prevailing direction (e.g. eastward) to the other (e.g. westward): the stratospheric guide is poorly established. Then, GW can bring the additional « kick» needed to set up a waveguide in a given direction, sometimes leading to multiple waveguides at different altitudes (see e.g. Fig. 19 of Blanc et al., 2019). More generally, GW induce small-scale heterogeneities leading to partial reflections that will direct energy towards the surface at distances not explainable by the mere consideration of refracting conditions in the geometric stratospheric waveguide. GW in the mesosphere can also induce ducting of infrasound waves through partial reflections; they

have vertical wavelengths down to values comparable with length scales of turbulence i.e. of the order of 100 m (e.g. Vorobeva et al., 2023). Finally, source energy estimation requires fine knowledge of the wind and temperature perturbations, hence of the GW field (e.g. Popov et al., 2022). While this is difficult to achieve without high-resolution observations of the atmosphere (e.g. using lidars—Baumgarten et al. 2010; Wing et al., 2021; Khaykin et al., 2020), advances in atmospheric modelling tools provide new paths for better investigation of the coupling between realistic GW fields and infrasound waves.

Several methods have been explored so far in the infrasound community to account for GW in atmospheric specifications for propagation modelling: parameterizations based on the GW universal spectrum (e.g. Gardner et al., 1993 as in Green et al., 2011; Vallage et al., 2021), stochastic parameterizations accounting for the intermittency of the GW field (e.g. de la Cámara et al., 2014 as in Cugnet et al., 2019), GW ray-tracing equations applied to a frequency spectrum (Drob et al., 2013) or 3D GW-spectrum model (Chunchuzov & Kulichkov, 2019). Working with models explicitly resolving a large part of the GW spectrum is another approach, which deserves to be considered given increasing computing means and we follow this path in this paper. GW parameterizations largely rely on approximations like the instantaneous and vertical-only propagation of the waves (see e.g. Plougonven et al., 2020). This may be detrimental to the realistic accounting of the GW impact on infrasound propagation. There are various sources and propagation conditions of GW (Fritts & Alexander, 2003), which can be highly intermittent (Hertzog et al., 2012). Hence infrasound detections are expected to be affected in different proportions by GW activity, across the globe and the IMS.

To our knowledge, efforts are missing to document and quantify the impact of GW across the whole network in a systematic way. It is often reminded that GW are misrepresented in models (under-resolved or poorly parameterized) and hence perturbation profiles must be added to simulated meteorological profiles in order to explain observations (Green et al., 2011, Vallage et al., 2021). Alternatively, dedicated models have been used to include GW effects on a case-study basis as mentioned above. It is possible, however, to provide a global picture of how GW impact infrasound propagation at a regional scale around each IMS infrasound station.

In this paper we present a method to assess that impact by working on surface transmission losses. In Sects. 2 and 3, we present the different datasets used in the study and the method put in place, respectively. In Sect. 4, we demonstrate GW-related variables derived from simulations at the Observatoire de Haute Provence in France, where lidar observations are available, and at the global scale for which satellite observations bring valuable constraints on GW activity. We then derive the amplitude of the GW impact at every single IMS infrasound station and highlight some general trend of this amplitude with respect to latitude across the IMS. Finally, in Sect. 5, we discuss the respective roles of the larger scale geometric guide and the GW activity itself, in the overall impact of GW on signal amplification.

2. *Data: Simulations and Observations*

2.1. *Simulated Fields: the DYAMOND Experiment*

The high resolution modelled fields come from simulations performed with the Icosahedral Nonhydrostatic Weather and Climate Model (ICON; Zängl et al., 2015) as part of the DYnamics of the Atmospheric general circulation Modeled On Nonhydrostatic Domains (DYAMOND) winter initiative (Stevens et al., 2019). The DYAMOND initiative is mainly dedicated to atmospheric simulations at global scale and storm-resolving resolutions (< 5 km) in order to assess the performance of different model configurations and different models in capturing tropospheric weather. It simulated weather for 40 days between 20 Jan and 1 Mar 2020. An essential part of the GW spectrum is explicitly resolved and no GW parameterization is used. Hence, lateral propagation of GW is accounted for, which is not the case for most GW parameterizations (Plougonven et al., 2020). It can be an important source of GW activity in a given region of the globe (Eichinger et al., 2023; Stephan et al., 2020). Convection and subgrid-scale orography are also not parameterized (Stephan et al., 2022). Model

configurations of DYAMOND extend into the middle atmosphere, giving the opportunity to investigate GW momentum fluxes in the stratosphere (Stephan et al., 2019a, 2019b). Results using these fields and more are highlighted in Stephan et al. (2022) and Köhler et al. (2023). We make an opportunistic use of this dataset to assess the impact of realistic GW at a global scale at each IMS station.

Two configurations of the ICON model were tested and they are named as ICON-nwp and ICON-sap following Stephan et al. (2022). Both simulations were initialized by the 20 Jan 2020 00:00 UTC analysis provided by the Integrated Forecasting System (IFS) of the European Centre for Medium-range Weather Forecast (ECMWF) and freely running with 6-hourly outputs. ICON-nwp uses the physics package of the operational ICON at 2.5 km horizontal resolution (Klocke et al., 2017) and is atmosphere only. ICON-sap uses different physics at 5 km horizontal resolution and the atmosphere is coupled with the ocean (Hohenegger et al., 2023). For more details on both configurations, we refer the reader to Stephan et al. (2022). The model top is at 75 km and a sponge layer starts at 45 km. For this reason, the fields are only considered up to 45 km to avoid including artificially damped waves. This is the main limitation of the present study.

2.2. *Lidar Observations at Observatoire de Haute-Provence, France*

The lidar at Observatoire de Haute Provence (OHP) has the longest time series for middle-atmospheric temperature on record (> 40 years) and was first presented in Hauchecorne and Chanin (1980). It is a key lidar station of the international Network for the Detection of Atmospheric Composition Change, NDACC (see e.g. Wing et al., 2021). The retrieval method for temperature profiles builds upon Rayleigh scattering, which causes the backscattering of the emitted photons. The number of collected photons is proportional to the atmospheric density, which is first retrieved before obtaining temperature using hydrostatic approximation. For details of the methods, refer to Hauchecorne and Chanin (1980) and Keckhut et al. (1993). Four one hour-averaged profiles per day (spanning the 18:00–22:00 UTC time slot) are available with a 150 m vertical step during the DYAMOND winter period. Vertical profiles of hourly temperature perturbations ΔT due to GW were also available. The filtering used to obtain hourly temperature perturbation profiles relies on the subtraction of the filtered nightly average temperature profile from the single temperature profiles. The nightly average profile is smoothed using a Hanning filter with an 8 km cut-off wavelength. 16-year long time series of such temperature perturbations (in the form of GW potential energy) were presented in Mze et al., (2014). These lidar perturbation profiles are used to assess our method for retrieving GW perturbations from the simulated fields, as presented in Sect. 3.1. Note that below 30 km, retrieval errors can occur in the temperature values because of aerosols biasing the processing. However, this should not affect the derived GW-induced perturbations themselves.

2.3. *Satellite Data: the GRACILE Dataset*

The use of satellite products was motivated by the need of further backing up the method for GW potential energy retrieval across the IMS using the DYAMOND outputs, hence not only relying on estimates at a single lidar site.

We use the GRAvity wave Climatology based on Infrared Limb Emissions observed by satellite (GRACILE; Ern et al., 2018) products, which are publicly available (Ern et al., 2017). It uses 3 years (2005–2008) of infrared observations from the High Resolution Dynamics Limb Sounder (HIRDLS) and 13 years (2002–2015) from the Sounding of the Atmosphere using Broadband Emission Radiometry (SABER) instrument. CO_2 emissions at 15 μm are observed in limb view mode and allow retrievals of atmospheric pressure and temperature. From these, GRACILE delivers different GW-related diagnostics of which we use GW potential energy (Ep) which is provided as a monthly average. We use zonal averages of the average, maximum and minimum Ep derived from both instruments with spatial resolution of 2.5° (HIRDLS) and 5° (SABER), where Ep is a climatology of monthly-averaged quantities.

3. Method: Atmospheric Specifications for Numerical Experiments

3.1. Extracting Gravity Waves Perturbations and Building Atmospheric Specifications

Vertical profiles of zonal (U) and meridional (V) winds, as well as temperature (T) are extracted at OHP and at every IMS station location. In order to assess the impact of atmospheric perturbations on the infrasound propagation the first step consists of preparing atmospheric specifications for propagation simulations. The general idea is to filter out small-scale perturbations that are characteristic of GW from the profiles, and build vertical profiles devoid of such perturbations (the background profile or mean flow). Propagation simulations using the latter profiles are compared to simulations using the full profiles at each station of interest.

For filtering, each 6-hourly output is linearly interpolated onto a regular vertical grid with a 1.5 km vertical step corresponding to the ICON average vertical resolution in the stratosphere in the DYAMOND simulations. Following previous studies focusing on GW (e.g. Baumgarten et al., 2015) a 3rd order Butterworth filter is applied to each field (U, V, T) with a given cut-off wavelength. A value of 15 km allows for realistic ΔT profiles compared to lidar and satellite products, as demonstrated in 4.1 and 4.2, respectively (as compared to 7 or 10 km, for instance). The background or filtered profile is then obtained (Fig. 2, black solid line). It is subtracted from the initial full profile (Fig. 2, red solid line), what leads to the GW perturbation profiles (ΔU, ΔV, ΔT) of which we consider the stratospheric part as illustrated in Fig. 3d–f. Note that ΔU and ΔV have opposite phases (compare Fig. 3d and Fig. 3e), which is consistent with the expected behavior from GW polarization relations (e.g. Fritts & Alexander, 2003).

In the following, we ignore the perturbations derived in the troposphere. We build hybrid atmospheric specifications where GW perturbations are not removed from the troposphere. This leads to a hybrid profile as depicted in Fig. 3 (top) where the black dashed line is smoothed (filtered) only in the stratosphere (above the temperature minimum). In doing so we avoid perturbation artefacts in the troposphere, not related to GW activity. These were occasionally obtained because of the tropopause and the jets beneath it as well as when low-level jets formed. These would bias the estimations of GW impacts on infrasound propagation. This hybrid approach is consistent with our focus on the impact of GW on the stratospheric guide at regional scales.

Finally, we restrict the propagation simulation to heights between 0 and 45 km, which are outside the sponge layer (45–75 km) of the model. We did not extrapolate the profiles in the upper stratosphere and MLT by using a climatology since this does not serve the purpose of quantifying the impact of the explicitly simulated GW in the stratosphere. In addition, such extrapolation would create perturbation artefacts in the upper stratosphere, at the boundaries between simulated and prescribed fields, respectively. This would alter the transmission loss differences obtained from the propagation simulations as explained below.

3.2. Atmospheric Waveguides and Propagation Simulations

Within the geometric acoustics approximation (high frequency approximation, i.e. assuming a slowly varying medium) the presence or absence of an infrasound waveguide can be assessed using effective celerity (c_{eff}) profiles, where c_{eff} is defined as:

$$c_{\text{eff}} = c + \vec{n} \cdot \left(U\vec{i} + V\vec{j} \right), \tag{1}$$

where $\vec{n}$ is the considered propagation direction and $\vec{i}$ and $\vec{j}$ are the unit vectors in the south-north and west–east directions, respectively. Acoustic rays coming from a source located at the surface can turn (refract) back towards the surface (z = 0) at a turning point of altitude z – hence creating a waveguide – if c_{eff} (z) > c_{eff} (z = 0) (e.g. Pierce, 2019), or equivalently if $C_{\text{ratio}} > 1$, where $C_{\text{ratio}}(z) = c_{\text{eff}}(z)/c_{\text{eff}}(z = 0)$.

The above framework cannot account for diffraction near the shadow zone and scattering or partial reflections of acoustic waves due to small-scale (high spatial frequency) atmospheric features. Hence, we use the parabolic equation (PE) to investigate realistic propagation conditions, provided within the ncpaprop

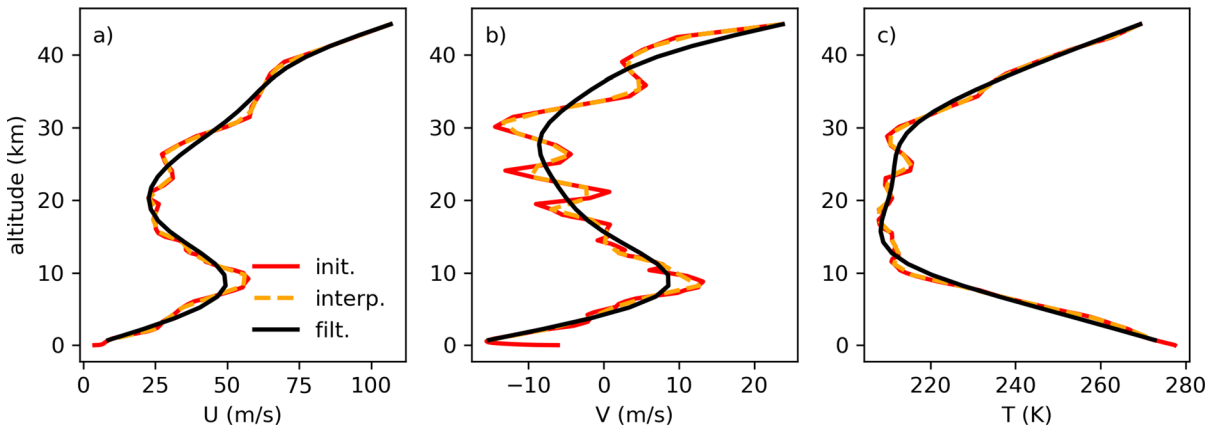

Figure 2
Vertical profiles of zonal wind U (**a**), meridional wind V (**b**) and temperature T (**c**) at OHP on 29 Jan 2020 18:00 UTC with ICON-nwp configuration. The original simulation output profile is in solid red, while the interpolated profile (vertical 1.5 km grid step) is in dashed orange. The resulting filtered background profile is in black

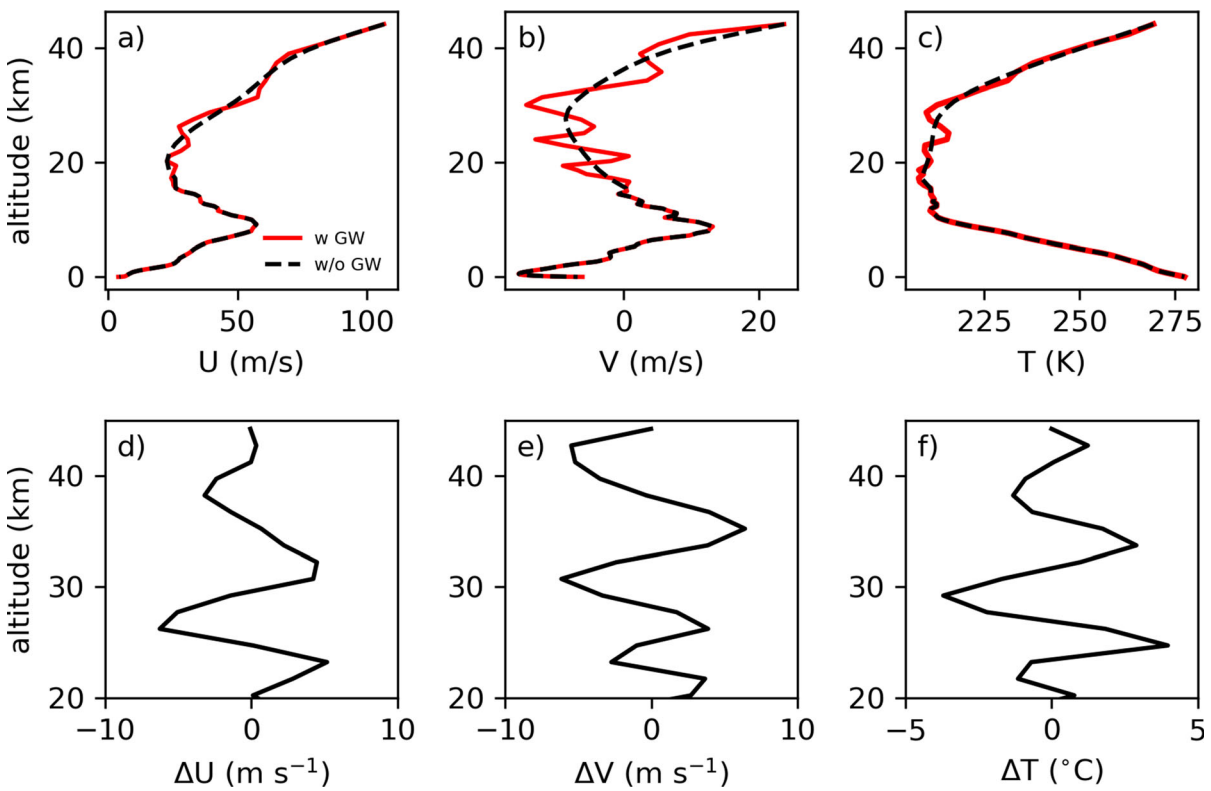

Figure 3
(Top) An example of two vertical profiles for winds (**a**,**b**) and temperature (**c**), between which the propagation simulations will be compared, in order to assess the impact of stratospheric GW on transmission losses. The hybrid background profile plotted in dashed black is devoid of GW only in the stratosphere (see text for details). The full (perturbed) profile is in solid red. (Bottom) Perturbation profiles in the stratosphere for the zonal wind (**d**), meridional wind (**e**) and temperature (**f**), obtained by subtracting the background profile from the full profile.

software (Waxler & Assink, 2019; Waxler et al., 2021). It uses the Sutherland and Bass (2004) model for acoustic signal attenuation, which provides frequency dependent attenuation coefficients driven by classical relaxation (translation and diffusion) and molecular relaxation (rotation and vibration). Out of plane scattering effects are not included in the model and planar terrain is assumed.

Using the atmospheric specifications described above (Fig. 3, top) we perform PE simulations across the whole period of the DYAMOND experiment at each IMS infrasound station, neglecting the first two days (spin-up time of the model runs). For a given model configuration, at each time step and at each station, two PE simulations are performed, with and without GW, respectively. For simplicity, the atmospheric specification is considered range-independent across the regional scales (500 km distance, allowing two shadow zones to fit in) and propagation is computed for all directions with a 2-degrees increment (0° corresponding to northward propagation) using wind and temperature profiles extracted from the model gridbox corresponding to the station location. In the calculations, we proceed by assuming that the source is at the station. Given the range-independency of the simulation, considering either westward or eastward propagation from the station, respectively, is strictly equivalent to considering respectively westward or eastward propagation from a source located away from the station and located on the diameter defining the direction of interest. To put it differently, characterizing eastward (resp. westward) propagation across 500 km as being propagation away from the station in the 45°–135° (225°–315°) angular sector, is strictly equivalent as characterizing propagation from a source located 500 km away from the station, towards the station, while being located in the 225°–315° (resp. 45°–135°) angular sector. The assumption of using the wind and temperature profiles at the station, across 500 km, shall be confronted to the typical horizontal wavelengths of atmospheric features. Planetary waves drive the stratospheric dynamics (e.g. see Chapter 12 of Holton & Hakim, 2013) and their typical horizontal wavelengths (> 1000 km) validate this approach. GW's horizontal wavelength range typically between 10 and 1000 km in order of magnitude in the MA so that using a range-independent approach bears physical sense for studying the impact of GW at regional scales (i.e. a few hundreds of km). This point, and more generally our working hypotheses, are further addressed in Sect. 5.3.

Surface transmission losses, TL (in dB), are obtained. TL is related to pressure signal amplitude (in Pa) as follows:

$$\mathrm{TL} = 20log_{10}(P/P_0), \tag{2}$$

where P represents the pressure signal amplitude at a given distance, and P_0 the amplitude at a reference distance of 1 km to avoid non-linearities. To quantify GW impact on the surface transmission loss, ΔTL is defined as follows:

$$\Delta\mathrm{TL} = \mathrm{TL}_{GW} - \mathrm{TL}_{w/oGW}, \tag{3}$$

where TL_{GW} and $\mathrm{TL}_{w/oGW}$ correspond to surface transmission loss derived using atmospheric profiles where GW are present and filtered out, respectively. Values of ΔTL of 6, 20, and 40 dB correspond to an increased signal amplitude by a factor of 2, 10, and 100, respectively. Simulations are performed at 0.1 Hz and 1 Hz, respectively, covering the two main orders of magnitude for acoustic frequencies of interest to IMS infrasound monitoring.

4. *Results: Gravity Waves Impacts on Surface Transmission Losses During Northern Winter*

4.1. *Gravity Waves at the Lidar Site of Observatoire de Haute-Provence, France*

Using the method described in Sect. 3.1 and the vertical profiles extracted in the simulated fields from the nearest gridbox to OHP location, we derive temperature perturbation profiles ΔT at OHP for both ICON configurations (ICON-nwp and ICON-sap). OHP lidar observations were acquired between 18:00 and 22:00 UTC. Hence, mean simulated vertical profiles of the temperature and of the absolute value of ΔT (|ΔT |) at 18:00 UTC are compared to the corresponding mean lidar profiles taken at 18:00 UTC in Fig. 4.

Both model configurations lead to temperatures consistent with the lidar observations in terms of

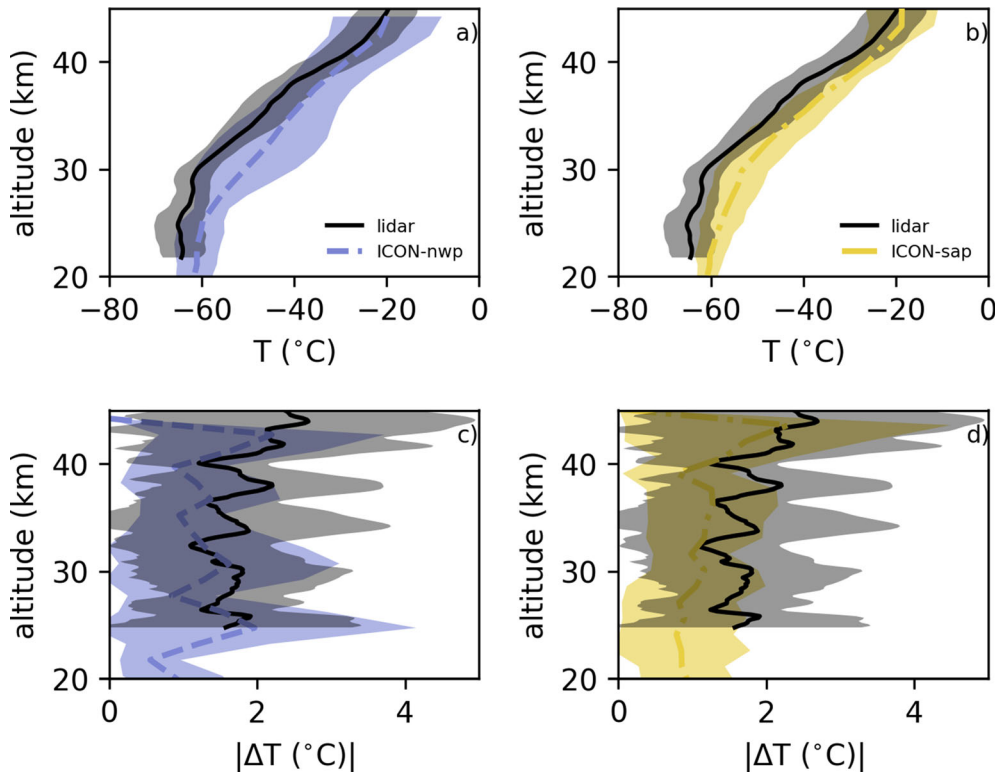

Figure 4
Mean vertical profiles of the temperature (**a**,**b**) and of the absolute value of the temperature perturbation (**c**, **d**). Lidar measurements (solid black line) are compared to simulations ICON-nwp (blue dashed line, in (**a**) and (**c**)) and ICON-sap (yellow dotted dashed line, in b and d) across the 16 dates (at 18:00 UTC) of the DYAMOND winter period when the lidar was operating. Shaded areas indicate ± one standard deviation from the mean

trend but also in terms of value, with less than 5 °C difference (except around 30 km, Fig. 4a and b). Similarly, perturbation profiles obtained from modelling are consistent with typical values deduced from lidar measurements (Fig. 4c and d). These results validate the simulations and the method proposed here, at least at the lidar site. Interestingly, the individual profiles used to derive each configuration's average temperature profile show larger biases in the second half of the simulation period (past 10 Feb 2020), as shown in the Appendix (Fig. 17). The free-running mode of the simulations may be responsible for the largest biases observed at the latest times, where the larger scale background fields are less and less determined by the initial conditions provided by the IFS analysis. This effect explains the notably larger bias around 30 km altitude (Fig. 17). Below 30 km, aerosols can also cause retrieval biases (Hauchecorne et al., 1992) and contribute to the overall difference observed with respect to the model. The perturbation profiles do not show the same trend in bias (Fig. 18 in the Appendix) but it appears clearly that the largest amplitudes of the perturbations are missed in general, possibly because of unresolved waves in the simulation. This is already suggested by the differences in the one-standard deviations plotted in Fig. 4c and d.

While it is difficult to differentiate between both configurations' results, it is interesting to look closer at vertical power spectrum densities (PSDs), as a function of $m/2\pi=1/\lambda_z$, where m is the vertical wavenumber.

Lower amplitudes for both simulation PSDs compared to the lidar PSD are consistent with the underestimation of |ΔT| amplitudes demonstrated in Fig. 4c and d (as shown in the Appendix, Fig. 19).

The observed spectrum displays the m^{-3} trend expected for the GW saturation regime (for large wavenumbers). Indeed, theoretical considerations and observations (e.g. Smith et al., 1987) demonstrate this behavior for gravity waves that break and transfer their momentum to the atmospheric medium (see also Fritts and Alexander (2003), for a review). This trend does not appear clearly in the simulations PSDs as in the lidar PSD (Appendix, Fig. 19). The coarser vertical resolutions of the modelled profiles (1.5 km) compared to the lidar (150 m) may explain this. To compensate for this, we extend the statistics for simulations PSDs by considering the whole DYAMOND winter period and not only the lidar observation times. Hence, Fig. 5 shows the simulations PSDs across 20 Jan – 1 Mar 2020 for ICON-nwp and ICON-sap, respectively, for all relevant fields at OHP. While the median simulated PSDs for temperature consistently show the trend in m^{-3} for ICON-nwp and ICON-sap (Fig. 5a) only ICON-nwp displays median PSDs following that trend for winds (Fig. 5b and c). The slope for ICON-sap is closer to -2. This suggests that the method fails at properly recovering GW perturbations for winds at OHP using ICON-sap simulation outputs. However ICON-sap does lead to GW PSD having the expected behavior at IMS stations (see Fig. 20 in the Appendix). Thus, it is relevant to consider the ICON-sap configuration along with ICON-nwp to investigate GW impact across the IMS.

4.2. *Gravity Waves Across the International Monitoring System: Comparison with Satellite-Based Estimations*

In order to validate the modelled global distribution of GW perturbations across IMS stations, we use the GRACILE products (Sect. 2.3) providing the GW potential energy E_p. It is derived using the GW perturbation temperature ΔT (see Sect. 3.1) as follows:

$$E_p = 1/2(g/N)^2\left(\Delta T/\overline{T}\right)^2,$$

where g is gravity, N is the Brunt-Väisälä frequency, and $\overline{T}$ the background temperature of the air parcel considered.

E_p is averaged across the altitude range 20–45 km, both in GRACILE and within the DYAMOND fields. Figure 6 displays the latitudinal distribution of E_p. It has been derived at each IMS station and averaged across the period of interest. The simulated value at OHP is also highlighted along with the corresponding value derived from the lidar measurements. The 95th percentile of the simulated E_p distribution is also shown to make parallel with the large lidar values. The average minimum and maximum of the satellite-derived E_p climatology for

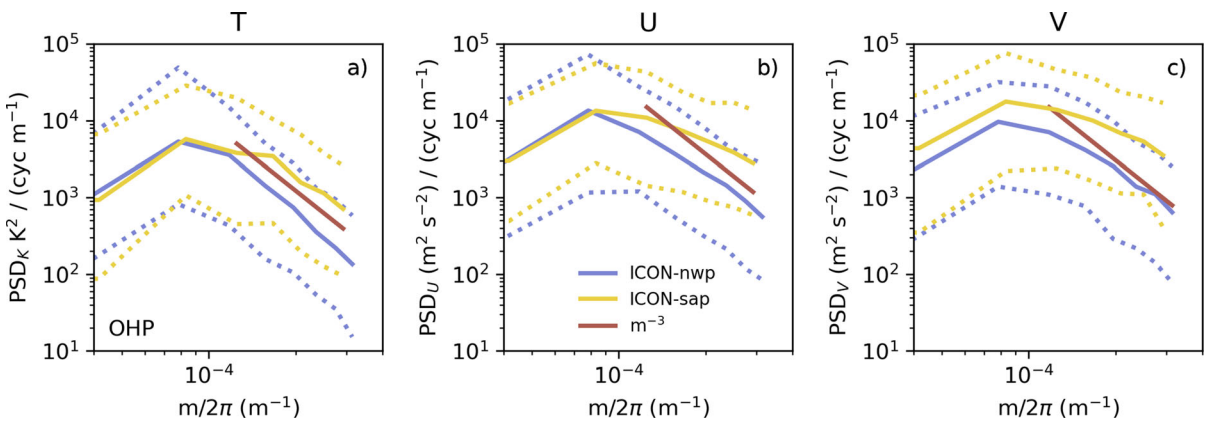

Figure 5
Vertical power spectrum density (PSDs) as a function of m/2π, where m is the vertical wavenumber, for T (**a**), U (**b**) and V (**c**), for ICON-nwp (blue) and ICON-sap (yellow), at OHP. PSDs are computed across the whole simulation period. Dotted lines show the 10th and 90th percentiles, respectively, and the brown solid line depicts the m^{-3} slope

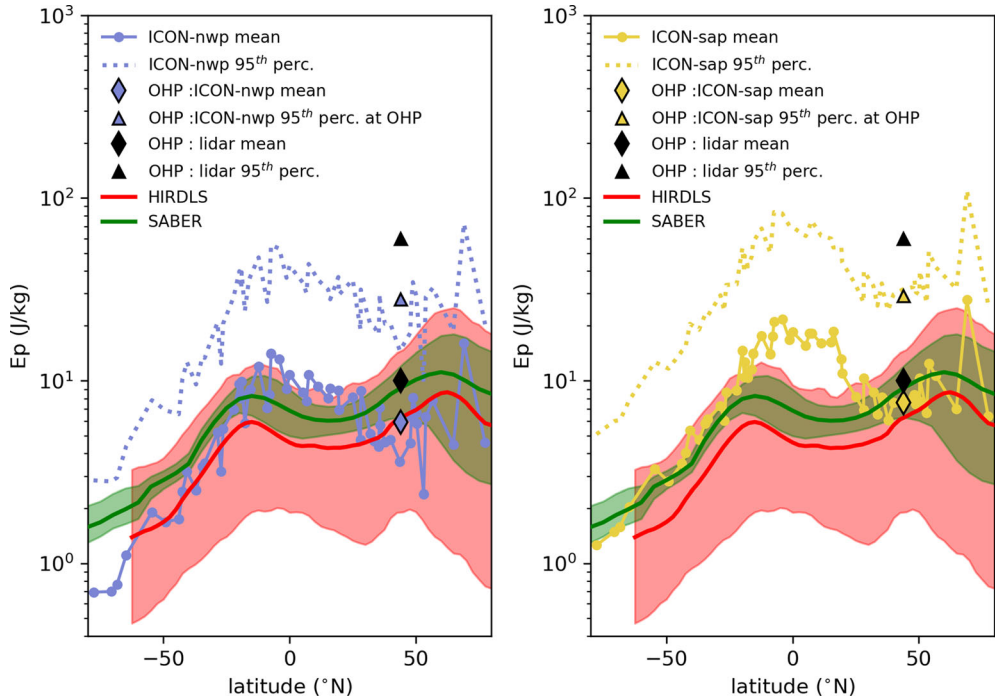

Figure 6
Zonally averaged latitudinal distribution of the time-averaged GW potential energy (Ep) derived using the GRACILE products, comparing with calculations based on the ICON-nwp (left) and ICON-sap (right) fields (solid lines). The colored diamond and triangle markers indicate values derived at OHP from simulations and the black equivalent markers relate to the lidar measurements. Potential energy is a 20–45 km altitude average. Satellite based calculations of Ep are plotted in green (SABER) and red (HIRDLS), respectively, with shaded areas referring to the range defined by the average minimum and maximum Ep

both instruments are indicated by the shaded area. The larger statistics for SABER (13 years) explains the narrower shaded area (in green) compared to HIRDLS (3 years) (in red). Owing to the winter season in the northern hemisphere, larger E_p values occur in the northern mid-latitudes than in the southern mid-latitudes. Weather systems, fronts, and hence non-orographic waves, are more active in the wintertime and GW activity increases due to stronger baroclinic jet-front systems (Plougonven & Zang, 2014).

Generally, both ICON configurations lead to a similar latitudinal trend with respect to observations. GW perturbations derived with the method presented here display a realistic latitudinal distribution. ICON-nwp leads to values in better agreement with GRACILE in the tropics and ICON-sap in the southern and northern mid- to polar latitudes of both hemispheres. Interestingly, both model configurations represent the observed decrease in GW activity from -10°N to 20°N. This overall match between model and observations across latitudes further supports that it is relevant to investigate GW impact on infrasound transmission losses across the IMS using the present method. Both model configurations are kept to investigate possible contrasting behaviors induced by the use of different model configurations.

4.3. *Examples of Gravity Waves Impacts on the Surface Transmission Loss*

To illustrate the impact of GW on infrasound propagation we focus on the surface transmission loss (TL) for particular cases. The method and the working hypotheses are described in Sect. 3.2.

Figure 7 summarizes how propagation is affected by the presence of GW perturbations at OHP, at a particular date and time. Propagation simulations

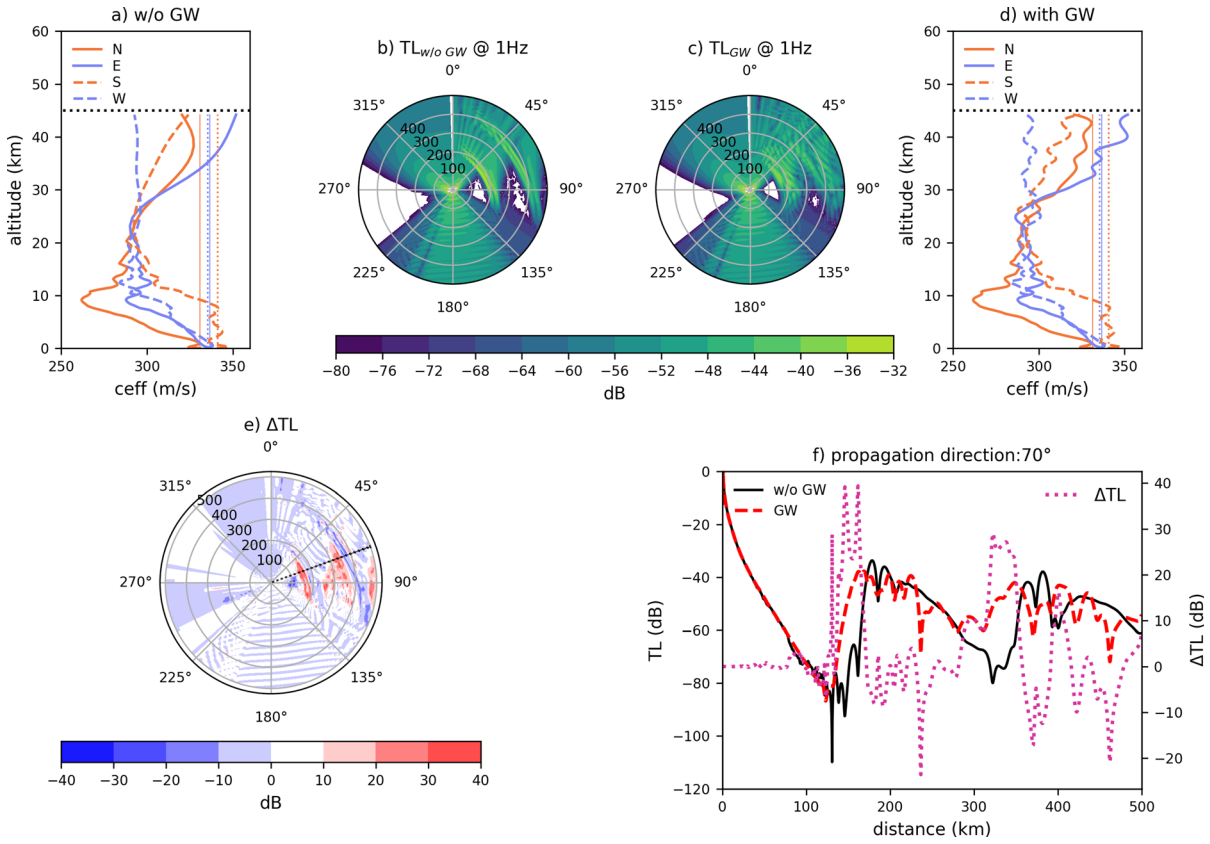

Figure 7

Tropospheric and stratospheric guiding at OHP. Propagation simulation performed at OHP, assuming a source at the station, on a specific date and time (29 Feb 2020 at 18:00 UTC), using atmospheric profiles without (**a**) and with (**d**) GW perturbations. In **a** and **d**, $c_{eff}(z)$ profiles are plotted for northward (N), eastward (E), southward (S), and westward (W) propagation, respectively. Vertical colored solid and dotted lines show the value of the effective celerity at the surface, where the source is. Vertical red and blue dotted lines are used as reference for southward and westward propagation respectively, while vertical red and blue solid lines are used for northward and eastward propagation, respectively. ICON-nwp is used here. **b** and **c** show the transmission loss (as a polar plot) for the profiles, respectively. The bottom row shows the transmission loss difference polar plot (ΔTL, dB) on the left (**e**). The dark dotted line shows the propagation direction for which transmission losses (solid and dashed lines) and ΔTL (purple dotted line) are plotted on the right subplot (**f**), as a function of distance. This example is of interest because it shows stratospheric guiding coming on top of tropospheric guiding (see text for details). Stratospheric GW change the way acoustic energy reaches the surface through the stratospheric guide in the shadow zones

were performed and TL maps derived. Figure 7a and d show c_{eff} (z) profiles that are plotted for the four cardinal directions and correspond to atmospheric specifications excluding and including stratospheric GW, respectively. Polar plots in Fig. 7b and c illustrate the propagation along all directions via the mapping of TL derived at 1 Hz. Northward propagation corresponds to 0°. Surface transmission losses are derived by ignoring ($TL_{w/o\ GW}$) or considering (TL_{GW}) GW and these are mapped in Fig. 7b and c, respectively. Figure 7e maps ΔTL and allows to readily focus on the contribution of stratospheric waves to TL since tropospheric features vanish in the subtraction (Sect. 3.1). Figure 7f shows plots of $TL_{w/o\ GW}$ (solid black line) and TL_{GW} (dashed red line) as a function of distance to the source in the particular direction indicated by the black solid line in Fig. 7e. The associated difference ΔTL is also shown in Fig. 7f (purple dotted line).

In the particular case of Figure 7 corresponding to OHP, the solid blue curve of the eastward effective celerity $c_{eff}(z)$ is crossing the vertical blue solid curve (at $\sim$ 35 km altitude) representing ground value for that effective celerity (Fig. 7a). This predicts a

stratospheric eastward waveguide according to the explanations given in Sect. 3.2. Two main tropospheric guides are predicted approximately northward (solid red) and southward (dashed red), at an altitude of $\sim$ 1 km and $\sim$ 200 m, respectively, where the corresponding $c_{eff}(z)$ profiles cross their respective ground value. The eastward stratospheric guide is characteristic of the northern mid-latitudes in winter. In Fig. 7b and c, approximately northward and southward propagation are indeed simulated (attenuations are low), respectively, due to the presence of tropospheric guiding in both directions as stated above. On top of this comes stratospheric guiding which translates as azimuthal arcs ranging between azimuths 0° and 100° in the polar plots (Fig. 7b and c) and corresponding to the stratospheric returns. The shadow zones of stratospheric propagation appear as darker (bluer) spaces between successive arcs. In Fig. 7c, TL_{GW} shows that the acoustic energy is more spread across the shadow zones. Figure 7e demonstrates indeed how acoustic energy distribution at the surface is influenced by GW, by mapping ΔTL. ΔTL is maximized in areas within the two shadow zones, around 150 km and 350 km, respectively. GW allow for significantly more acoustic energy to penetrate the shadow zones. A given direction is indicated with a dotted line on the polar plot of Fig. 7e, for which TL and ΔTL are plotted in Fig. 7f (ΔTL purple dashed line). This figure shows the increased amount of energy in the shadow zones by up to 40 dB (a factor of 100 in signal amplitude) at this specific time. Note that in the absence of an established (or almost established) geometric guide the impact of GW oscillations on transmission loss is not significant. For instance, oscillations of the $c_{eff}(z)$ profiles corresponding to southward or westward propagation (Fig. 7d) do not lead to significant difference in transmission losses in those directions (Fig. 7e).

Figure 8 shows an example featuring a different impact of GW, at IS37 (in Norway). Here GW create stratospheric guiding in directions between the northwest (315°) and the northeast (45°) (Fig. 8c). Indeed, shadow zones are clearly identified inbetween the azimuthal arcs going from 315° to 45° (and crossing the 0° line) and where TL values are maximized. Figure 8e shows the corresponding values of ΔTL ranging from 40 dB (light pink), between $\sim$ 15° and $\sim$ 45°, to 80 dB (dark pink and red) between 315° and 0°. This stratospheric guiding comes in addition to tropospheric guides in the northeast and in the southeast directions (in the lowest layers of the troposphere). They were readily found without including GW contributions (Fig. 8b). This example is important as it reminds that GW can lead to the formation of new geometric guides, thus allowing propagation in directions not primarily receiving acoustic energy at all. Note that, as for the previous example at OHP, significant oscillations in the $c_{eff}(z)$ profile corresponding to directions with no stratospheric geometric guiding (for instance for westward propagation – dashed blue line – in Fig. 8d) do not lead to increased TL values (Fig. 8e).

Figure 9 shows an example for a station in the southern hemisphere (IS08, in Bolivia) where dominant stratospheric winds are westward and no tropospheric guiding is present. GW act by spreading more acoustic energy through the shadow zones (Fig. 9f). Stratospheric GW, which are clearly seen in Fig. 9d on the $c_{eff}(z)$ profiles, play a major role in changing the propagation conditions in the main directions of the propagation where geometric guiding is set (westward but also in the northwest and southwest directions), filling the shadow zones. Despite GW being present in the $c_{eff}(z)$ profiles corresponding to northward (N), eastward (E) and southward (S) propagations (Fig. 9d), these waves do not increase TL values between 0° and 180° in azimuth (Fig. 9e). This is because geometric guiding is absent for these propagation directions.

In order to summarize the impact of GW at a given station during the winter period investigated (20 Jan–1 Mar 2020), we average TL values between azimuths 45° and 135° for eastward propagation and between 225° and 315° for westward propagation. In order to avoid compensating effects a distinction is made between occurrences of positive and negative ΔTL values. An increase of acoustic energy ($\Delta TL > 0$) at a given distance is obtained at the expense of the loss of energy in other areas ($\Delta TL < 0$) or of energy not initially trapped in the stratosphere (escaping upwards). The words “gain” and “loss” are used to describe these respective occurrences. To avoid very large values of ΔTL due to GW allowing for transmission where no signal is initially expected

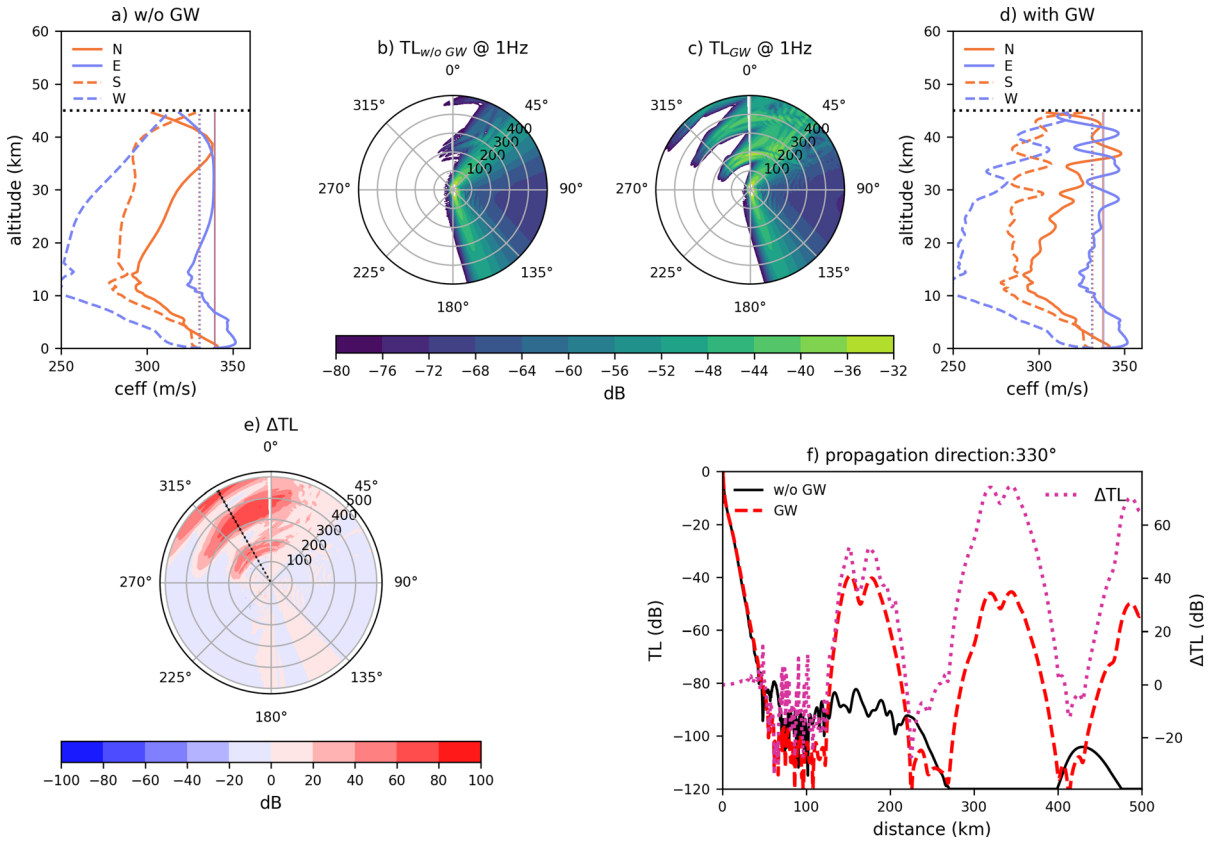

Figure 8

Stratospheric geometric guiding allowed by gravity waves at IS37. Same as Fig. 7 but for station IS37 on the 26 Feb 2020. In this example, gravity waves are responsible for additional guiding in directions (north-west to north-east) otherwise not impacted by the stratospheric propagation

without GW (as in the example of Fig. 8), we focus on instances where $TL_{w/o\ GW}$ is initially above -60 dB (i.e. the attenuation is not greater than a factor of 1000 in amplitude). Thus, we decide to quantify how areas already getting some signal given the large-scale propagation conditions are affected by GW in terms of that signal's amplitude. Results are shown in Figs. 10, 11 and 12 for the stations OHP, IS37 and IS08, respectively. Average gain and loss as a function of distance are shown along with their respective standard deviation throughout the winter period.

The average shadow zones' locations are identified at places close to the local maxima of the gain, as observed in Figs. 10 to 12. There, GW increase signal amplitude through partial reflections and strengthening of the main guides. At OHP the maximum average gain is around 5 dB (factor of 1.8 in amplitude) in both directions while it is $\sim$ 10 dB (factor of 3) and $\sim$ 6 dB (factor of 2) at IS37 in the westward and eastward direction, respectively. At IS08, 25 dB maximum average gain (factor of 18 in amplitude) is derived in the direction of the main guide (westward) while less than 5 dB is derived in the opposite direction. Different patterns of the gain and loss are illustrative of the various geographical locations, which determine whether, and by how much, GW perturbations affect TL.

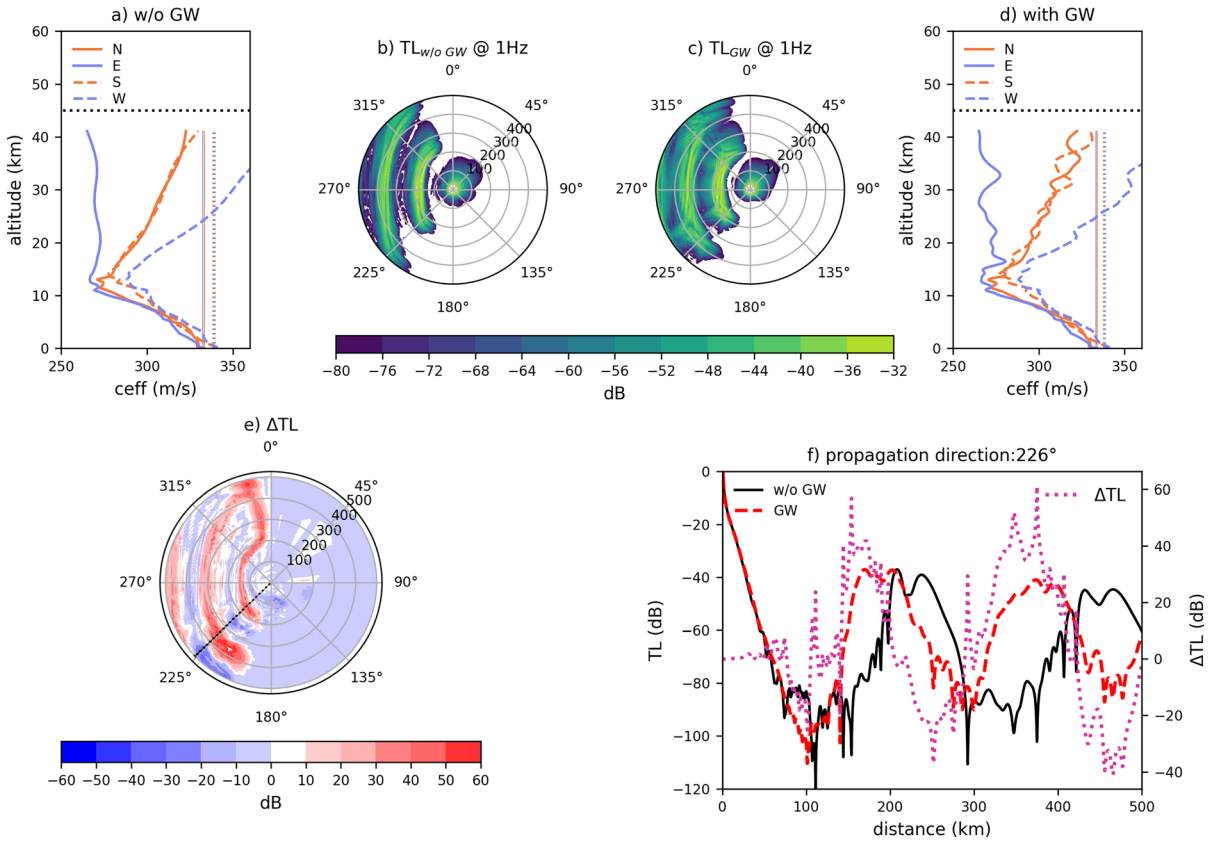

Figure 9
Stratospheric guiding only, at IS08. Same as Fig. 7 but for IS08 on the 23 Jan 2020. In this example, only stratospheric guiding is playing a role in regional propagation and GW spread the acoustic energy across the shadow zones

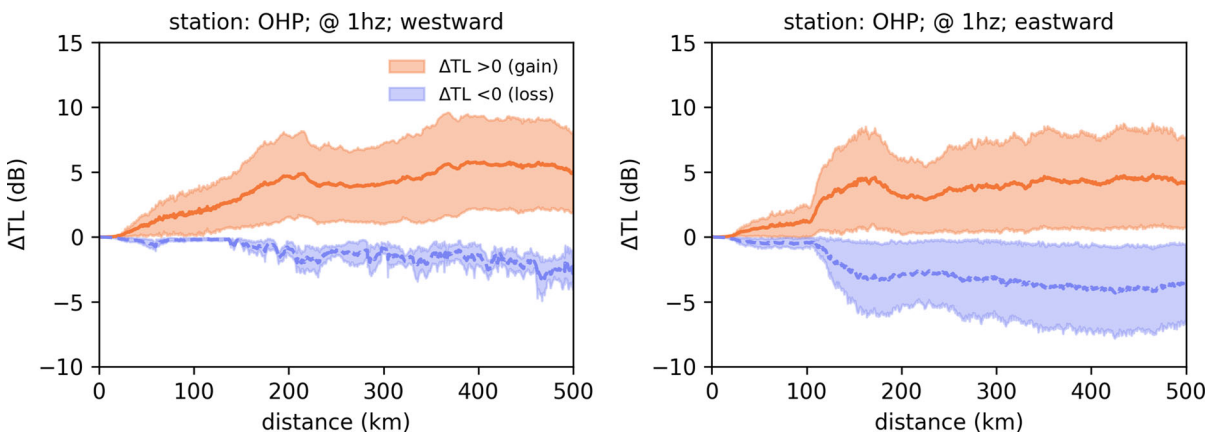

Figure 10
Average TL difference (ΔTL) at 1 Hz, between TL_{GW} and $TL_{w/o\ GW}$ through 20 Jan–1 Mar 2020, as a function of distance, at OHP. ICON-nwp is used. Positive and negative ΔTL values are grouped together before averaging in order to plot gains ($\Delta TL > 0$) and losses ($\Delta TL < 0$), separately. The average is derived by restraining azimuths to westward propagation (range 225° to 315° in azimuths) (left) and eastward propagation (between 45° and 135°) (right)

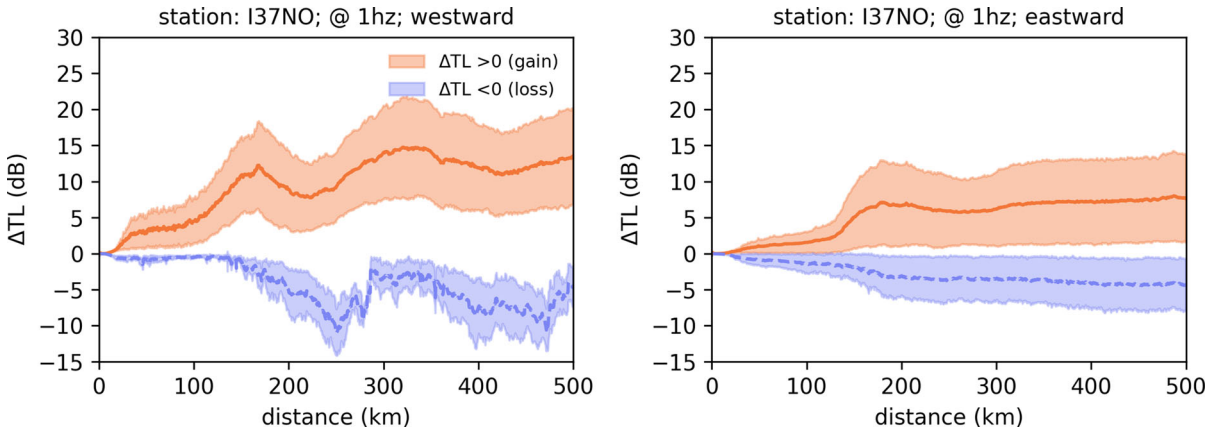

Figure 11
Same as Fig. 10 but for IS37 (Norway)

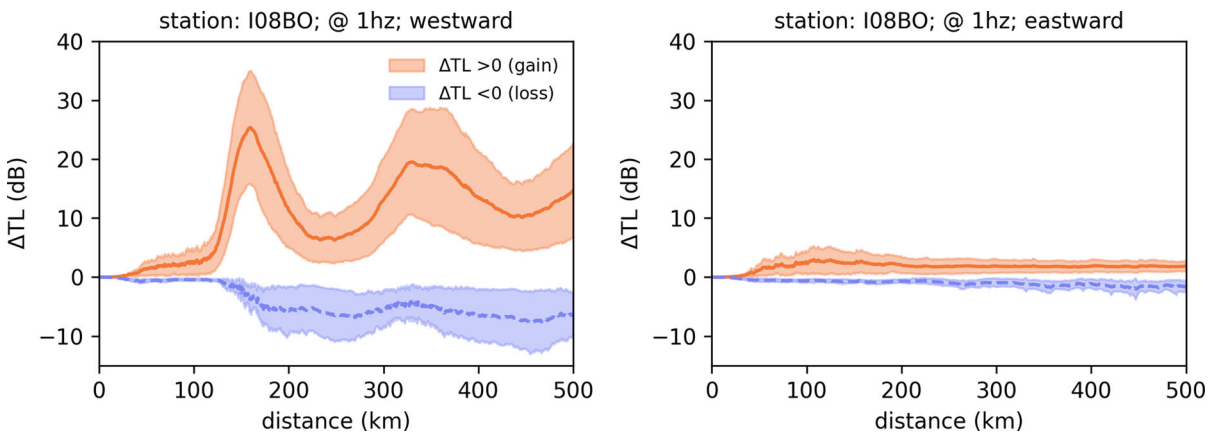

Figure 12
Same as Fig. 10 but for IS08 (Bolivia)

4.4. *Impact of Gravity Waves Across the IMS During Northern Winter*

To investigate systematic effects or trends across the IMS in the impact of GW on TL values during northern winter, we plot the maximum average gain (occurrences of $\Delta TL > 0$) and maximum average loss ($\Delta TL < 0$) found within 100–250 km from all stations as a function of latitude for both ICON configurations. This range includes one of both areas where the largest gains due to GW are derived, the shadow zones, and here we consider the region around the first stratospheric return. However, similar (and sometimes even larger) values of ΔTL can be found when considering the shadow zone around the second stratospheric return (i.e. within the range 300–450 km). Focusing on the first shadow zone to characterize global trends of GW-related gains across the IMS allows in principle to be less biased by our range-independency approach for propagation and we stick to this range unless stated otherwise. Hence,

systematizing the approach demonstrated in Sect. 4.2 to all stations we select the maximum average gain and loss within 100–250 km. Some considerations of regional averages within 100–500 km distance are also presented by the end of this subsection. Plots for each IMS station are shown in the Appendix for both propagation directions (Fig. 21 and Fig. 22, respectively) where a marker indicates the maximum average gain that is picked to draw the synthetic plots described in the following. Recall that gains and losses of acoustic energy at the surface are only considered where the transmission loss without GW

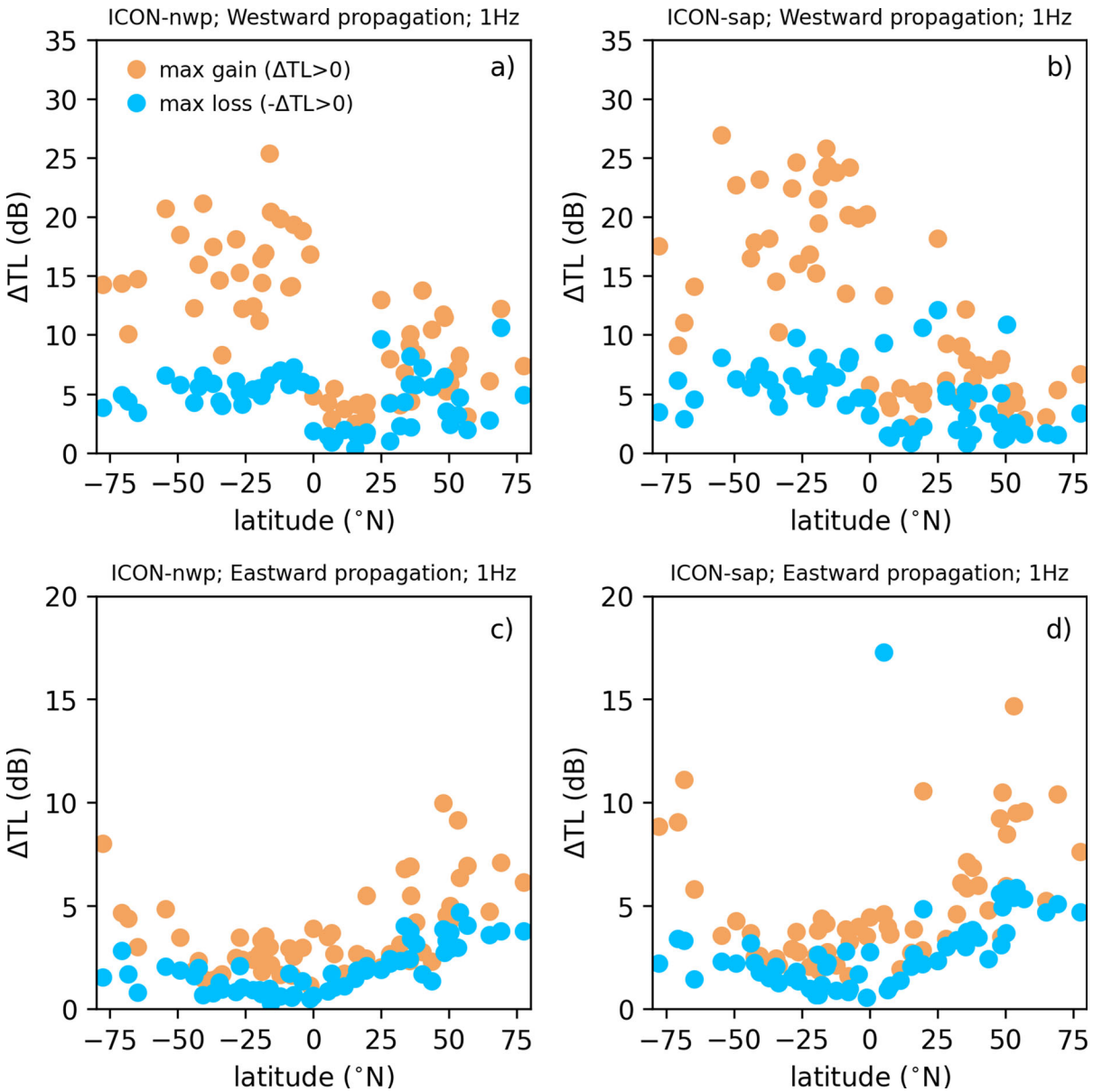

Figure 13
Maximum ΔTL reached within 100–250 km (in the shadow zone, around the first stratospheric return) from the station as a function of latitude (considering all IMS stations) for both model configurations ICON-nwp (**a**,**c**) and ICON-sap (**b**,**d**), considering westward (**a**,**b**) and eastward (**c**,**d**) propagation

is above − 60 dB, i.e. where the signal attenuation is not greater than a factor of 1000 in amplitude.

We consider westward (Fig. 13a et b) and eastward (Fig. 13c et d) propagation as in the previous section and plot the maximum gain or loss recorded within 100–250 km from the station at 1 Hz. The average main GW impact on TL occurs prominently for westward propagation as opposed to eastward propagation. At southern latitude stations, average gains of 10 to 25 dB are derived (up to a factor of 20 in amplitude) when considering westward propagation. Both model configurations lead to similar values and conclusions, making the assessments more robust. Average gains remain largely below 5 dB for eastward propagation for the southern stations and below 10 dB for northern stations. A clear decrease of the GW impact is observed from the southern hemisphere to the northern hemisphere (Fig. 13a et b).

For eastward propagation ΔTL is increasing from southern to northern latitudes (Fig. 13c et d). The contrasting (eastward vs. westward) trends in GW impact on propagation and ΔTL cannot be related to the northward increase in GW activity demonstrated in Fig. 6 in a straightforward manner. This is addressed in the discussion part.

At 0.1 Hz, the aforementioned variations and large GW impacts almost vanish, as shown in Fig. 14, which summarizes the gain and loss for both propagation directions for the ICON-nwp configuration. A similar conclusion is drawn with ICON-sap (not shown). The main reason for this is the lesser sensitivity of lower infrasound frequencies (larger wavelengths) to the small-scale perturbations whose effect is highlighted here.

The above results focus on the first shadow zone where GW impacts on TL are the largest. Focusing on the second shadow zone around the second stratospheric return would lead to similar behavior and range of values. But the impact of GW is not limited to the shadow zones and the average gain across a larger region (100–500 km) lies in the range 2–15 dB for westward propagation and in the range 1–7 dB for eastward propagation (not shown). This range is 0–5 dB with respect to losses in both directions. Hence, the main difference between considering maximum average gain in the range 100–250 km and overall average gain in the range 100–500 km is tributary to the shadow zones where GW impact is the largest as illustrated by single station figures (see Appendix, Fig. 21). The average increase or decrease in amplitudes caused by GW

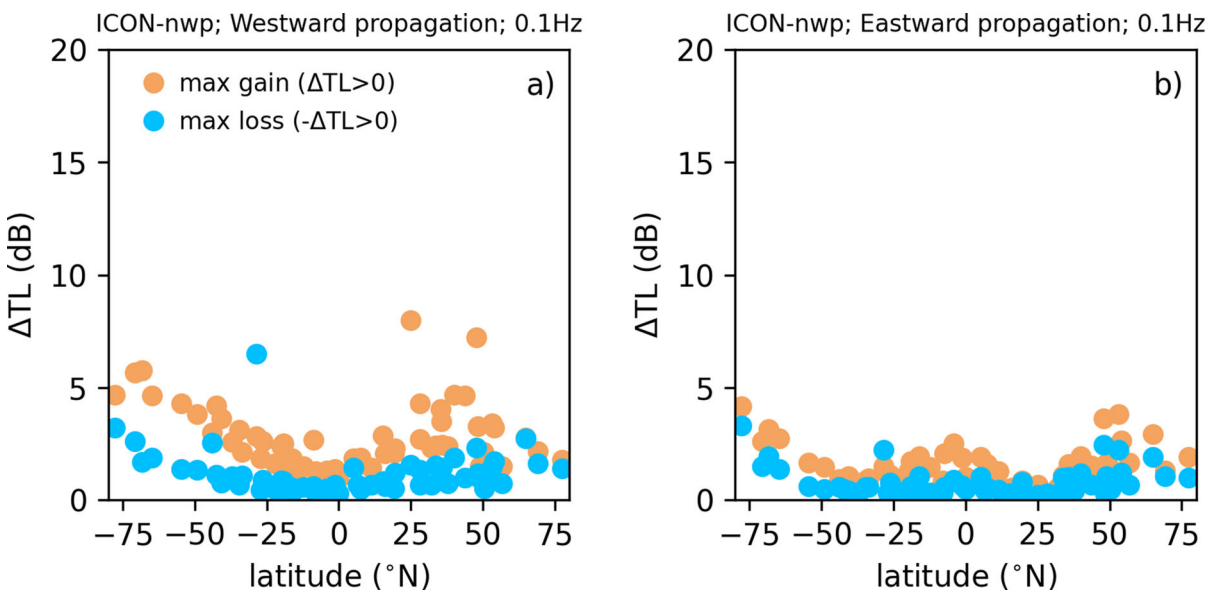

Figure 14
As Fig. 13 but for ICON-nwp only and for both propagation directions, westward (**a**) and eastward (**b**)

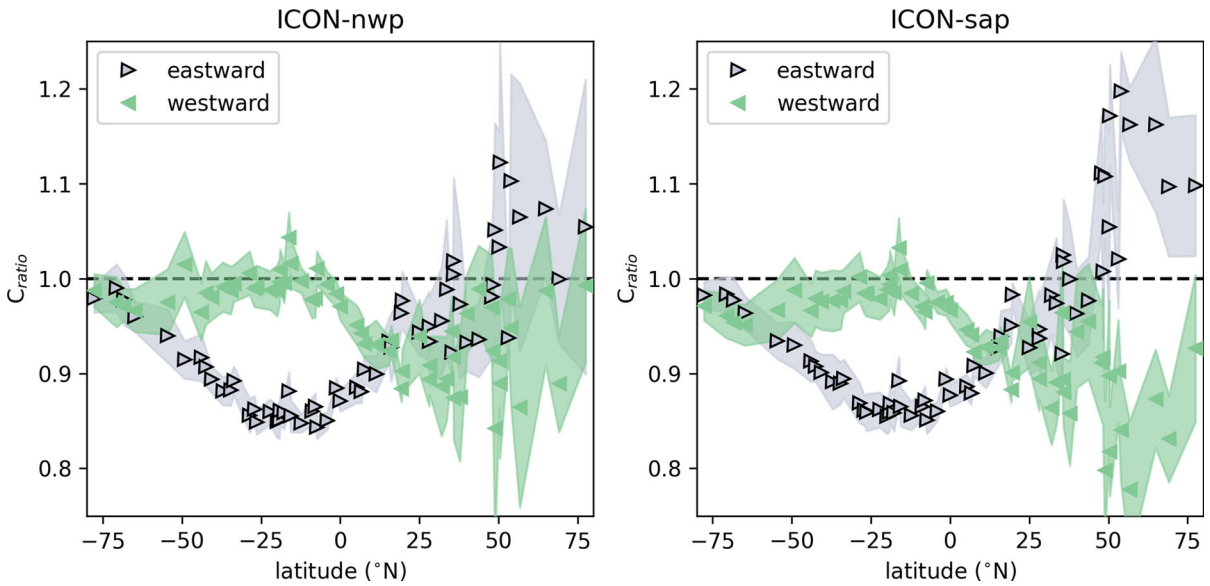

Figure 15
Latitudinal distribution (across IMS stations) of the C_{ratio} value (see text for details) for both westward propagation (green leftward triangle) and eastward propagation (grey rightward triangle), for ICON-nwp (left) and ICON-sap (right), during the DYAMOND northern winter period. Shaded areas indicate one standard deviation from the C_{ratio} value plotted with the markers (see text for the derivation of that standard deviation)

across regional distances (100–500 km) in northern winter is thus lower than a factor of 10, when not specifically focusing on either of the shadow zones. However, note that some differences still remain between the summer (southern) hemisphere (gain being within 5–15 dB) and the winter (northern) hemisphere (gain being within 2–10 dB) for westward propagation.

Finally, gains and losses attributable to GW share a similar range of values as demonstrated by Fig. 13 (1 Hz) and Fig. 14 (0.1 Hz). This appears not to be true for cases where GW impacts are the largest and for instance in the southern hemisphere for westward propagation (Fig. 13a and b). Computed gains due to GW are larger than losses by a few dB (eastward propagation, Fig. 13c and d) to 10–15 dB (westward propagation, Fig. 13a and b). Figure 12 (left), which focuses on the westward propagation at a southern hemispheric station (IS08), clearly shows how the maximum gain and loss differ within 100–250 km from the source. Figure 9e also shows the larger positive amplitudes of ΔTL compared to the negative amplitudes of ΔTL. The gain increase at the surface is not at the expense of a loss increase in other areas at the surface. In the cases where GW impacts are the largest, GW will allow to significantly trap additional energy, which otherwise escapes into upper layers (when excluding GW). This especially applies to westward propagation during the austral summer, when $C_{ratio} \sim 1$, suggesting that GW are strengthening almost established guides.

5. Discussion

5.1. Role of the State of the Geometric Guide in the GW Impact

We demonstrate different impacts of GW on TL between the southern and northern hemisphere during

northern winter, as well as distinct trends in that impact across latitudes. We focus on the strength of the westward and eastward stratospheric waveguides, respectively. This approach points at a dependency of the GW impact on the state of that large-scale (geometric) waveguide.

Figure 15 shows the state of the infrasound geometric guide via the coefficient C_{ratio} (defined in Sect. 3.2), for both westward and eastward propagations, for ICON-nwp (Fig. 15, left) and ICON-sap (Fig. 15, right) configurations. The plotted C_{ratio} is derived as follows. First, the maximum value within the altitude range 30–45 km is found for each time step and for each azimuth. Second, that maximum value is time-averaged for each azimuth and standard deviation is also retained. Finally, the maximum of these time-averaged maxima is picked in the azimuth range 45–135° (for eastward propagation) and 225–315° (for westward propagation), respectively. The corresponding standard deviation is also retained and the ± one standard deviation from the mean is also plotted in Fig. 15. Note that the average latitudinal distribution of C_{ratio} is almost unchanged whether profiles including or excluding stratospheric GW are used. This means that the general effect of GW is not the proper creation of new geometric waveguides (as illustrated in Fig. 8), rather the formation of atmospheric features increasing the amount of reflected acoustic energy and/or strengthening almost established guides (as in Figs. 7 and 9).

As expected, both ICON configurations simulate an eastward guide dominant in the winter (northern) hemisphere and a westward guide dominant in the summer (southern) hemisphere, owing to the usual stratospheric jets orientation during northern winter. Both model configurations simulate equivalent waveguides in the southern hemisphere until the northern mid-latitudes ($\sim$ 45°N) where they start differing. ICON-nwp's westward and eastward guides are closer in strength than ICON-sap's. For the latter, eastward propagation is clearly favored at the expense of westward propagation at northern mid to polar latitudes (Fig. 15, right).

Figure 6 demonstrated the overall increased GW activity (amplitude) as latitude increased, except from a transient decrease in the northern equatorial and tropical regions. This decrease can be explained by the GW activity being largest in the southern tropical and equatorial regions due to the southward position of the intertropical convergence zone where (deep) convection gives rise to GW activity in the stratosphere (e.g. Alexander et al., 2000).

To explain, however, the largest GW-related gains derived for transmission losses at high to tropical southern latitudes in the westward direction (Fig. 13a and b), one needs to consider the average state of the geometric guide in that direction. The latter has values of $C_{ratio} \sim 1$ (Fig. 15), which means that the guiding is not well established. This allows GW to play a greater role in favoring reflections of additional acoustic energy towards the surface. Despite of having relatively higher energy in the northern hemisphere compared to mid- to high southern latitudes, GW will have on average more impact on transmission loss in the southern hemisphere for the westward propagation, for which $C_{ratio} \sim 1$.

For eastward propagation C_{ratio} displays clearly unfavorable values to guiding (with a minimum value of 0.85 reached around 23° S, Fig. 15), hence the much more negligible gains in amplitude allowed by GW for this propagation direction (Fig. 16). The increased C_{ratio} for eastward guiding in the northern hemisphere with values approaching one (25–50° N) and exceeding one (50–80° N) explains the larger impact of GW on transmission losses in the northern hemisphere compared to the southern hemisphere. However, the gains in amplitude remain lower than for the southern hemisphere and the westward direction, by 10 dB or more.

5.2. *Mapping the Gravity Wave Impact at IMS Infrasound Stations*

Overall, our analysis leads to similar conclusions with respect to GW impact on surface transmission losses across the IMS, whether performed with

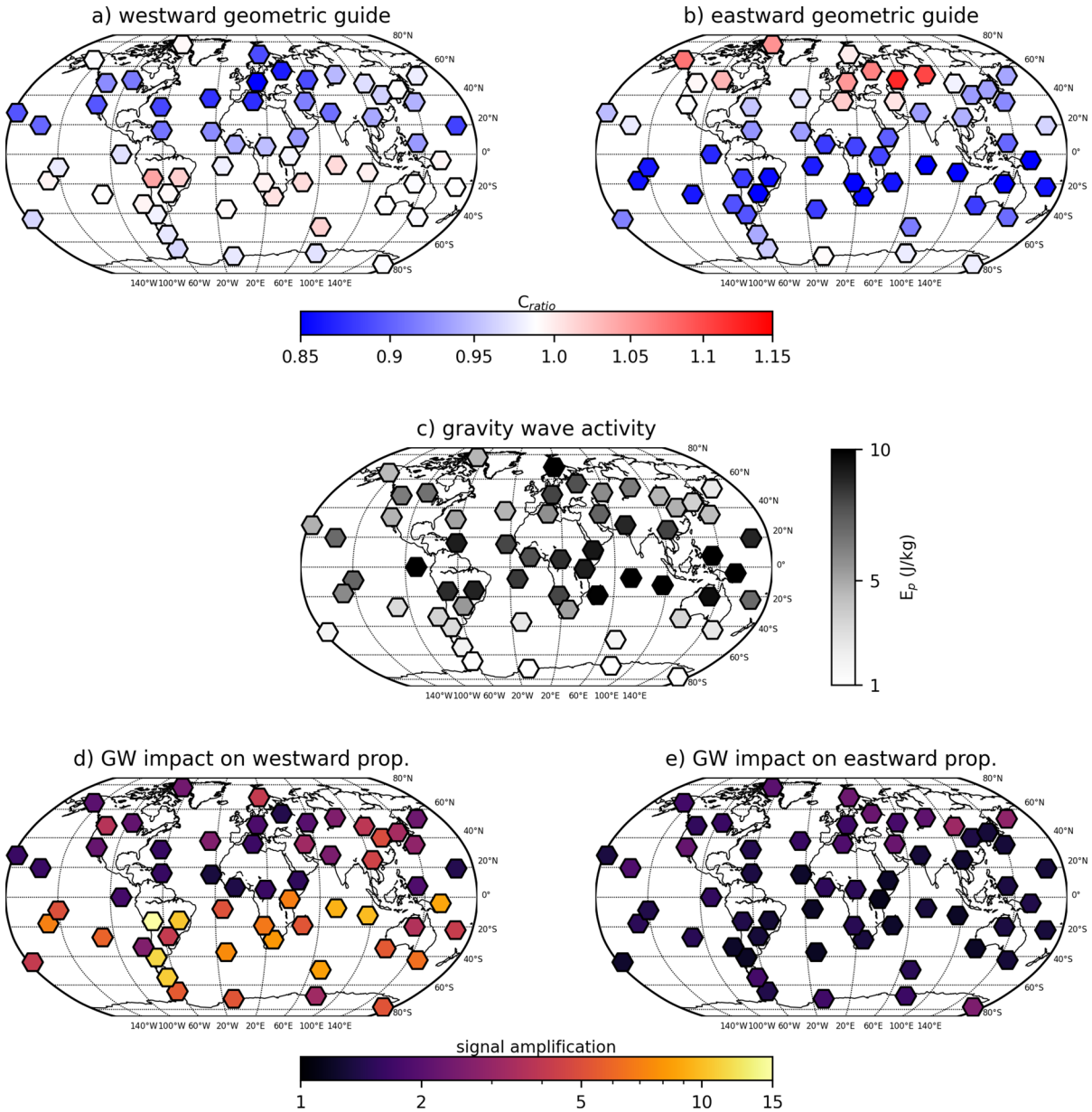

Figure 16

Mapping across IMS stations of key variables derived for northern winter 2020 and discussed in the study using ICON-nwp outputs, (**a**,**b**) C_{ratio}, (**c**) E_p and (**d**,**e**) the gain $\Delta TL > 0$ converted into signal amplification (see text for details) (focusing on the maximum average in the 100–250 km range, near to the first stratospheric return, in the shadow zone) for westward propagation (**d**) and eastward propagation (**e**), respectively

ICON-nwp or ICON-sap configurations. Figure 16 maps several variables addressed in this study for ICON-nwp. ICON-sap shows similar trends and relative distributions of the various variables (see Fig. 23 in the Appendix), albeit with slightly larger signal amplification with respect to GW impact as already demonstrated in Fig. 13).

The effective celerity ratio (C_{ratio}) is shown in Fig. 16a and b for opposite propagation directions respectively, the GW potential energy (Ep) in Fig. 16c and the derived impact of GW on TL for opposite directions in Fig. 16d and e, respectively. A striking feature remains that the highest derived impact of GW on amplitude is in the high and mid southern latitudes, i.e. not where GW amplitude is the largest but rather where GW activity combines with an average stratospheric jet not clearly set in a given direction ($C_{ratio} \sim 1$).

In Fig. 16d and e, we converted the average transmission loss difference ΔTL into an equivalent amplification of the signal amplitude (i.e. focusing on cases where $\Delta TL > 0$) using Eqs. (2) and (3). Note that the arithmetic average of ΔTL corresponds to a geometric average of the pressure signal amplitude ratios. In virtue of the arithmetic mean-geometric mean inequality, the average amplification factor plotted in Fig. 16d and e is actually a lower limit of the actual (arithmetic) average amplification factor. Yet, it provides a valuable order of magnitude to present the results in a more intuitive fashion. The GW impact on infrasound propagation at regional scales will vary from one station to another reminding the necessity to account for GW effects in a realistic manner, where both the state of the waveguide and the actual GW activity are represented. An amplification of 5 to 15 in signal amplitude in the shadow zone is demonstrated across the southern hemisphere for the westward propagation while this factor lies around 2–4 in the northern hemisphere. This amplification is much smaller for eastward propagation disregarding the considered hemisphere with values generally below two (Fig. 16e).

It is noteworthy that a similar contrasting impact is not observed when comparing northward (315°-45°) and southward (135°–225°) propagation directions (see Appendix, Fig. 24). An amplification factor of less than 5 is observed for any of both directions with no specific pattern. This fact is consistent with C_{ratio} maps not displaying any specific pattern globally. The eastward or westward jets are not zonally symmetric, mainly due to the existing planetary scale (Rossby) waves which cause successive accelerations and decelerations of these currents, leading to their meanders, especially in the northern hemisphere due to strong orography contrasts. This explains the alternating northward and southward guiding present in the northern hemisphere (Fig. 24a and b).

5.3. Limitations and Prospects for Progress

The main limitation of the investigation is, first, the consideration of a model top at 45 km height, meaning the stratosphere is not entirely covered. However restraining to explicitly resolved GW allows us to include the effect of lateral propagation which is usually missed in most models relying on GW parameterizations (Plougonven et al., 2020), while it appears as an important source of GW at any place on the globe (Stephan et al., 2019a, 2019b; Eichinger et al. 2023).

Second, the vertical resolution used in the simulation experiments leads to the consideration of GW with a vertical wavelength of 3 km or more. Infrasound waves of interest to the IMS (0.02–4 Hz) have wavelengths between $\sim$ 100 m and $\sim$ 20 km so that a part of the relevant GW spectrum that can interact with the acoustic waves and that could contribute in further ensonifying the shadow zones, is missed. However, these missed wavelengths belong to the saturated part of the GW spectrum and their amplitude would be much lower than the wavelengths of the resolved part because of the marked decrease of energy as function of increasing wavenumber (see Fig. 5 and, in the Appendix, Figs. 19 and 20). As a

consequence, their impact on the average gains derived in the shadow zones would probably be smaller than that of the resolved GW. This remains to be investigated. Finally, a major difficulty would be to account for both GW and turbulence at the same time when addressing the impact of small-scale perturbations (see e.g. Vorobeva et al., 2023).

Third, range-independent simulations across 500 km are performed. As addressed in Sect. 3.2, GW may have all kinds of horizontal wavelengths, however short horizontal wavelength are more easily reflected so that GW with horizontal wavelength greater than 10 km are usually considered important for middle atmospheric dynamics (Fritts & Alexander, 2003). This partly justifies a range-independent approximation to work out GW impact at regional scales (a few hundreds of km) using atmospheric specification (hence GW activity) above the station. Keeping all these limitations in mind, we nonetheless demonstrate a method describing the contrasting impact of GW on attenuation or amplification of infrasound signals through the IMS in the winter (20 Jan–1 Mar 2020). Updating such an approach within a model covering the whole middle atmosphere with GW explicitly resolved in the vertical and in the horizontal would complement this first investigation that provides a general view of how small-scale perturbations matter for IMS monitoring activities globally.

Finally, reproducing such work for other seasons, in summer and during the equinoxes, would complement the picture given by Fig. 16d and e. During the equinoxes, the zonal stratospheric waveguides in both hemispheres are not firmly set in any given direction (C_{ratio} takes values above or below 1.0) so that the average signal amplification due to GW could potentially be significant in both hemispheres at the same time (as opposed to the picture given by Fig. 16d). However, it would depend on the global distribution of GW activity as well.

6. Conclusion

In this paper, we use state-of-the-art simulations of the ICON model within the DYAMOND project to investigate the impact of stratospheric GW on the infrasound propagation across the IMS during northern winter. The period covered by the DYAMOND winter experiment is 20 Jan to 1 Mar 2020.We focus on surface infrasound transmission losses at regional scales (< 500 km) at each infrasound station. This attempt is the first of its kind to bring some global view of the expected impact of GW on signals detected by the infrasound component of the IMS, and to document the factors driving that impact.

We perform propagation simulations using atmospheric specifications including and excluding the GW contribution in the stratosphere, respectively. The simulated GW, which are extracted from the background field, are backed up by high-resolution atmospheric measurements at a lidar site, and by coarser global observations obtained from satellite products.

We derive the GW impact on surface transmission loss, considering the main eastward and westward propagation directions. We demonstrate that the largest impact does not necessarily occur at places where GW activity is the largest, but rather where the large-scale geometric waveguide is not well established. For the considered period, this mainly occurs for the westward southern stratospheric jet, which is weaker than the eastward one in the northern hemisphere during (northern) winter.

We demonstrate the contrasting impact of GW across the IMS network. The greatest impact of GW on transmission loss occurs in the southern hemisphere from polar to tropical latitudes for westward (225–315°) propagation. There, GW amplify signals by at least 5 to 15 in the shadow zone, on average, against a factor of 2–5 in the northern hemisphere for the same propagation direction. Eastward propagation is much less affected by GW given the large-scale guide, which is clearly unfavorable (southern hemisphere) or clearly favorable (northern hemisphere) during northern winter. Signal amplification in the eastward shadow zone is less than 4 and generally less than 2. These amplification factors represent the maxima obtained in the first shadow zone, but similar conclusions would apply by considering the shadow zone near the second stratospheric return.

It is important to note that GW will affect the whole transmission loss regionally, by potentially amplifying signals within hundreds of kilometers around the source, by a factor of less than 10 on average. The contrasting qualitative impact of GW on transmission loss, when comparing hemispheres or directions of propagation, still holds when considering the average regional impact (across 100–500 km from the station) rather than the impact in the shadow zones. GW impact is clearly dominating at higher frequencies (1 Hz) while lower frequencies (0.1 Hz) are far less affected (at most 5 dB in the shadow zone, i.e. a factor of less than 2).

Understanding the impact of GW across the IMS is important for detection capability considerations and event analysis, and this work is a first step in that direction. Operational atmospheric models are usually not capable of simulating explicitly realistic amplitudes of GW. They rely on GW parameterizations to compensate for their horizontal resolution ($\sim$ 10 km). The sponge layers implemented are also a drawback for realistic amplitudes to be simulated in the stratosphere, as they usually start as low as 25–30 km (e.g. the IFS model, the operational ICON model). Improving and extending a similar work to atmospheric simulations with improved vertical resolution, higher model top and sponge layer, and across other seasons, as well as including horizontal variations, will allow broadening the conclusions drawn here and include GW from the upper stratosphere to the MLT. State-of-the-art three-dimensional atmospheric models extending to the upper atmosphere, like the upper-atmosphere version of the ICON model, UA-ICON (Borchert et al., 2019), are an interesting route to follow. On the one hand, this model can run at a very high resolution ($\sim$ 1 km), thus allowing in principle to ignore GW parameterization, although GW wave effect may not even converge at 1 km (Polichtchouk et al., 2023). On the other hand, UA-ICON also benefits from recent development of gravity wave parameterization accounting for non-dissipative interactions between the mean field and the GW field (Bölöni et al., 2021; Kim et al., 2021). The latter are not accounted for by usual GW parameterizations, as the ones implemented in meteorological operational models.

Acknowledgements

The authors are grateful to the two anonymous reviewers for their very careful reading of the manuscript, which helped clarify and improve its content. CL thanks M. Ern for pointing at the GRACILE dataset.

Author Contributions C. L. designed the study, performed the analysis, and wrote the manuscript. C. C. S. handled the atmospheric simulation dataset, provided the expertise needed to use these data and expertise on GW, contributed to the design of the study, and to the writing of the manuscript. A. L. P. contributed to the infrasound propagation simulation design, and to the writing of the manuscript. A. H. handled the lidar data and provided the expertise on these data as well as on GW. Y.-H. K. reviewed the manuscript and contributed to discussions in the use of modelling data. U. A. contributed to the writing of the manuscript and to the GW-related expertise. G. B. reviewed the manuscript and contributed to discussions in the use of modelling data.

Funding

C.C. Stephan was supported by the Minerva Fast Track Program of the Max Planck Society. DYAMOND data management was provided by the German Climate Computing Center (DKRZ) and supported through the projects ESiWACE and ESiWACE2. The projects ESiWACE and ESiWACE2 have received funding from the European Union's Horizon 2020 research and innovation programme under grant agreements No 675191 and 823988. This work used resources of the Deutsches Klimarechenzentrum (DKRZ) granted by its Scientific Steering Committee (WLA) under project IDs bk1040 and bb1153. UA thanks the German Research Foundation (DFG) for partial support through CRC 301"TPChange" (Project-ID 428312742, Projects B06 "Impact of small-scale dynamics on UTLS transport and mixing" and B07 "Impact of cirrus clouds on tropopause structure") and through the

CRC 181 “Energy transfers in Atmosphere an Ocean” (Project Number 274762653, Projects W01 “Gravity-wave parameterization for the atmosphere” and S02 “Improved Parameterizations and Numerics in Climate Models.”). YHK and UA thank the German Federal Ministry of Education and Research (BMBF) for partial support through the program Role of the Middle Atmosphere in Climate (ROMIC II: QUBICC) and through grant 01LG1905B.

Data Availability

The GRACILE dataset can be downloaded at the following link: https://doi.pangaea.de/https://doi.org/10.1594/PANGAEA.879658. The DYAMOND winter experiment outputs can be requested by contacting the ESiWACE coordination team: https://www.esiwace.eu/the-project/past-phases/dyamond-initiative.

Declarations

Conflict of interest The authors have no relevant financial or non-financial interests to disclose.

Appendix

See Figs. 17, 18, 19, 20, 21, 22, 23 and 24.

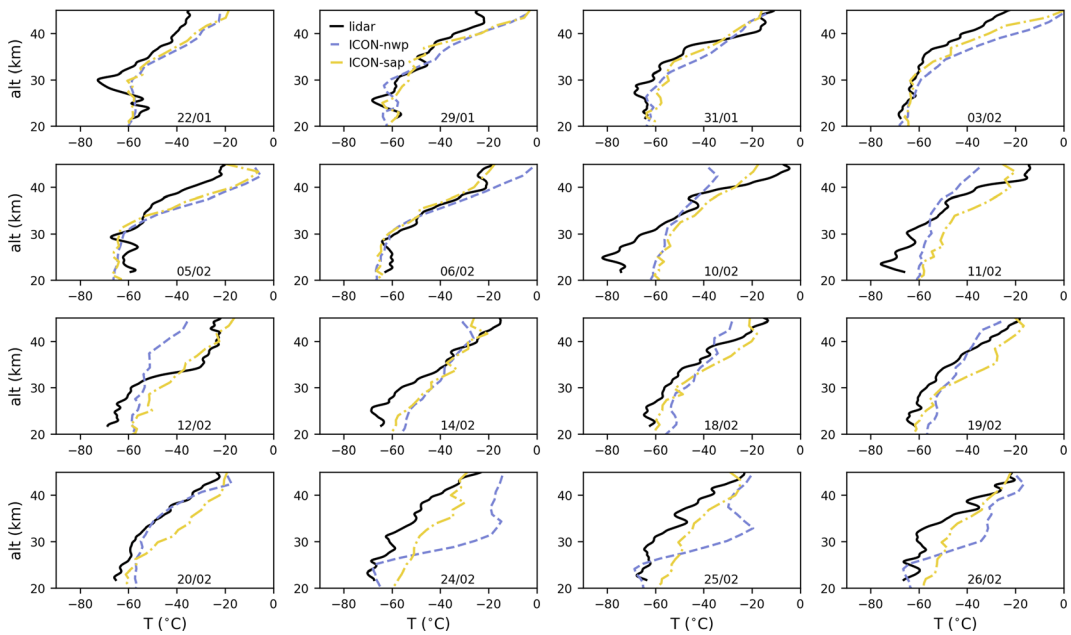

Figure 17
Single vertical profiles from the lidar (solid black line) and the simulations (ICON-nwp with blue dashed line and ICON-sap with yellow dotted-dashed line) used to compute the average profiles shown in Fig. 4a and b

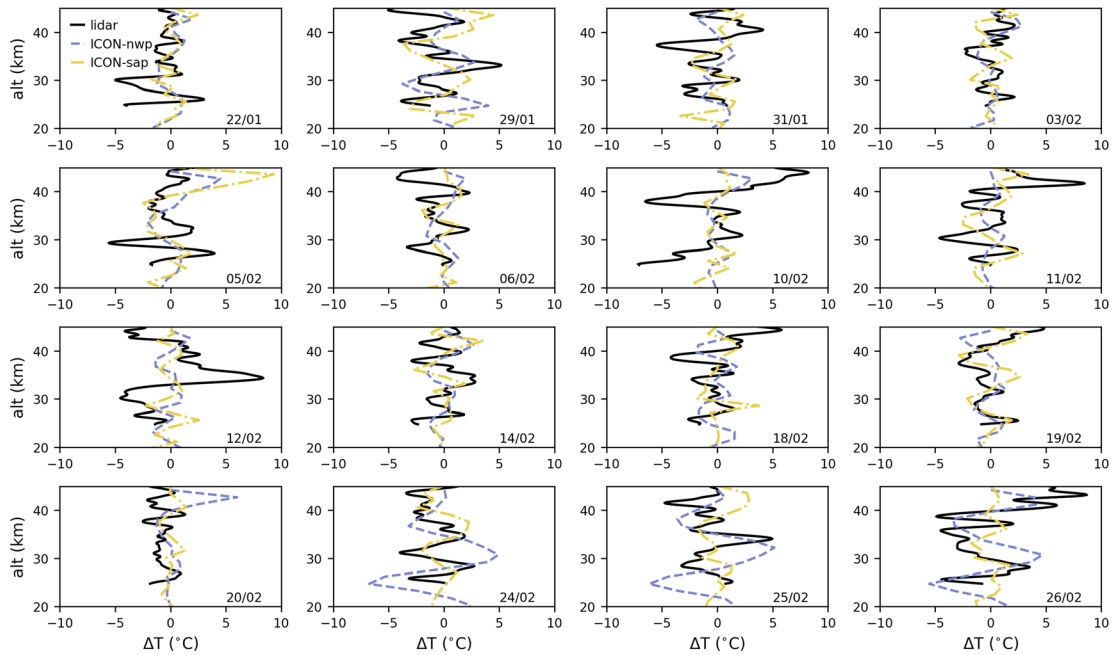

Figure 18
Same as Fig. 17 but for the perturbation profiles. Their absolute value is averaged to obtain the profiles shown in Fig. 4c and d

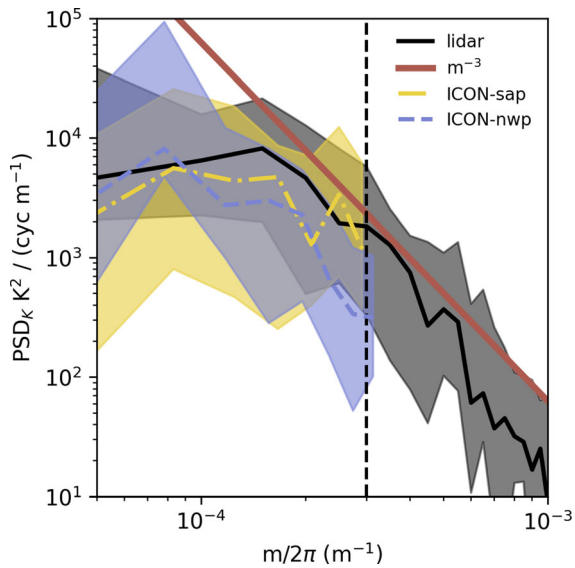

Figure 19
Vertical power spectrum density (PSDs) of temperature as a function of m/2π, where m is the vertical wavenumber. The PSD is computed as the median of the PSDs of each temperature profiles on the days of lidar observations at OHP, using the one-hour average (18:00–19:00 UTC) lidar profile, and considering the 18:00 UTC output for both ICON simulations. The shaded area corresponds to the range between the 10th and the 90th percentiles. The brown solid line indicates the m^{-3} slope generally expected for vertical spectra in the saturated part of the GW spectrum. The vertical dashed line points at the lower wavelength that can be investigated within the simulated profiles, i.e. 3 km

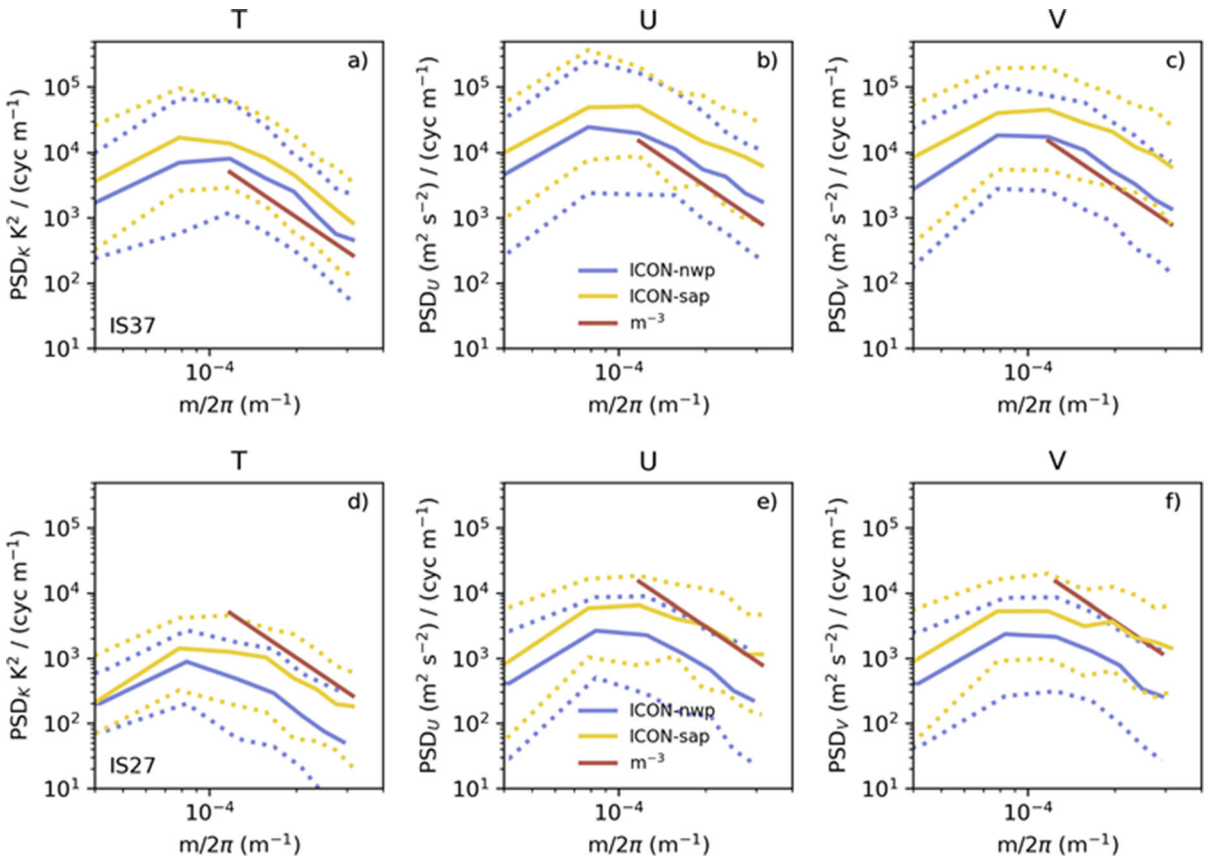

Figure 20

Vertical power spectrum density (PSDs) as a function of m/2π, where m is the vertical wavenumber, for T (**a**,**d**), U (**b**,**e**) and V (**c**,**f**), for ICON-nwp (blue) and ICON-sap (yellow), at IS37 in Norway (**a**–**c**) and IS27 in Antarctica (**d**–**f**). PSDs are computed across the whole simulation period and not only at lidar observation times as in Fig. 5. Dotted lines show the 10th and 90th percentiles, respectively, and the brown solid line depicts the m^{-3} slope

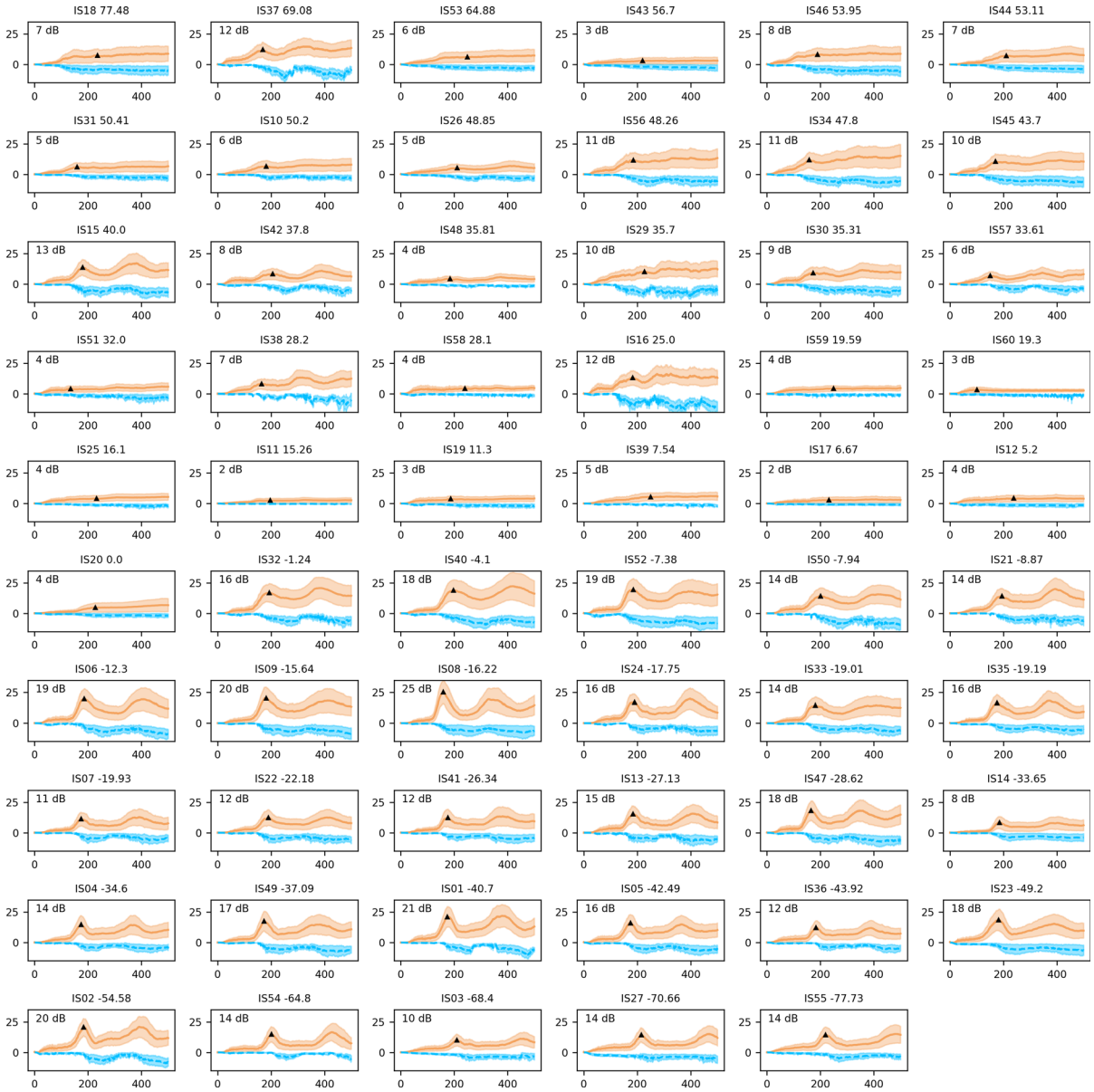

Figure 21

Average value of ΔTL as a function of distance to the station for each IMS station (sorted by decreasing latitude from the top left corner to the bottom right corner), for westward propagation (225°–315°), obtained with ICON-nwp. Positive values of ΔTL (corresponding to gain or, equivalently, signal amplification) are plotted in orange, and negative values of ΔTL (corresponding to loss, or signal attenuation) are plotted in blue. The maximum average value within the range 100–250 km from the station is marked with a black filled triangle in the shadow zone, and its value is denoted for each station in the top left corner of each subplot

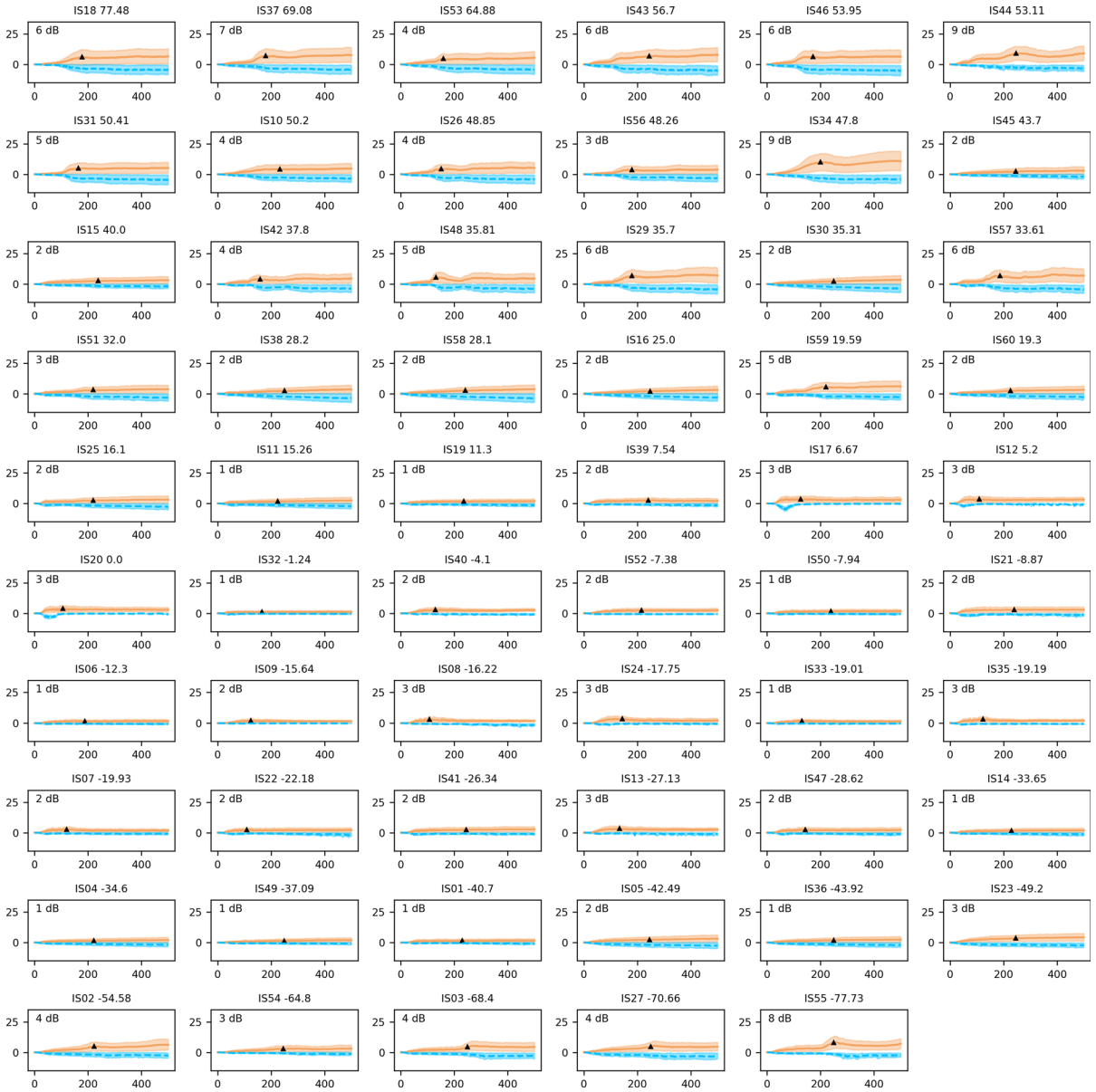

Figure 22
As for Fig. 21 but for the eastward (45°–135°) propagation

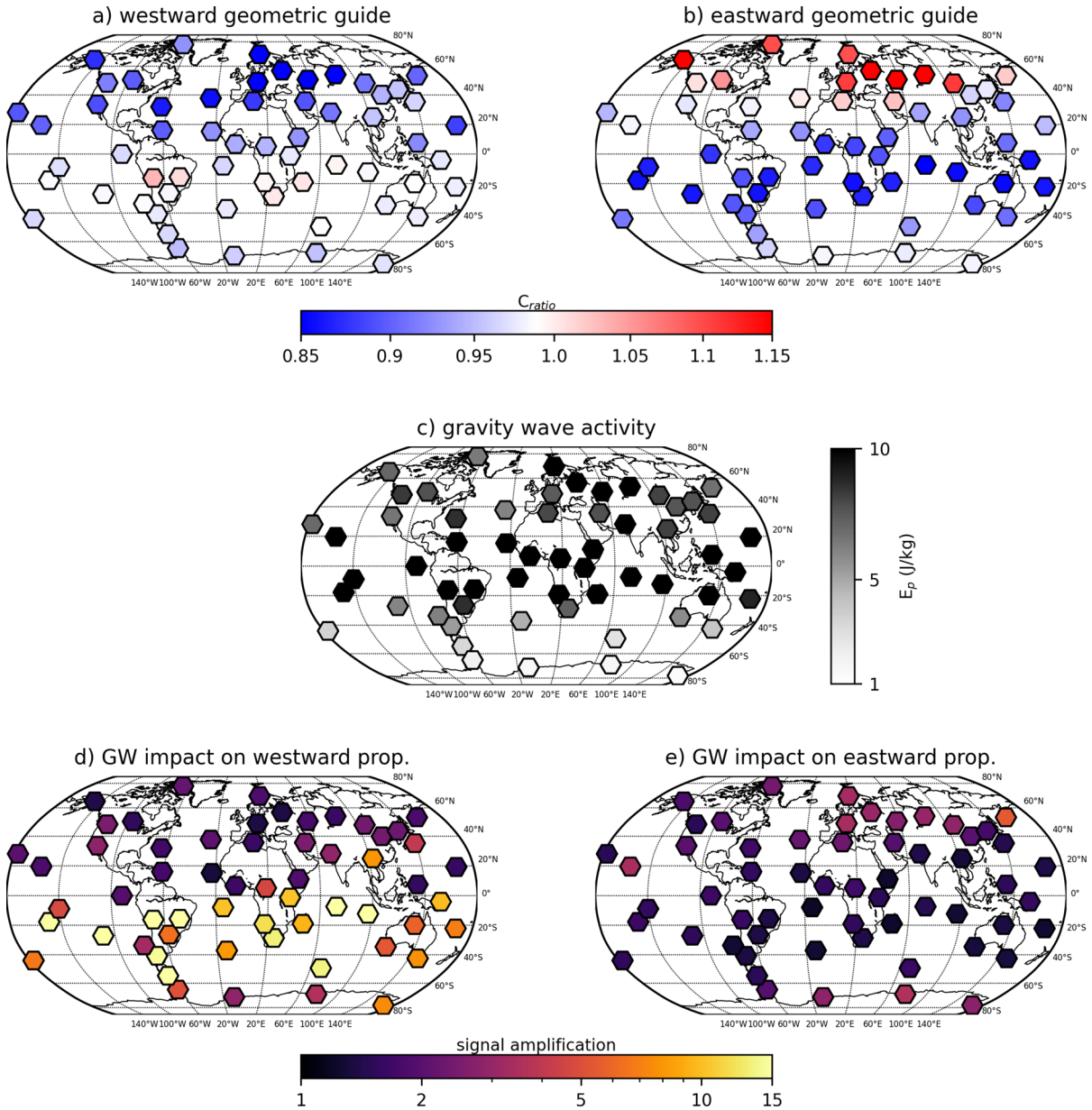

Figure 23
As Fig. 16 but for ICON-sap configuration

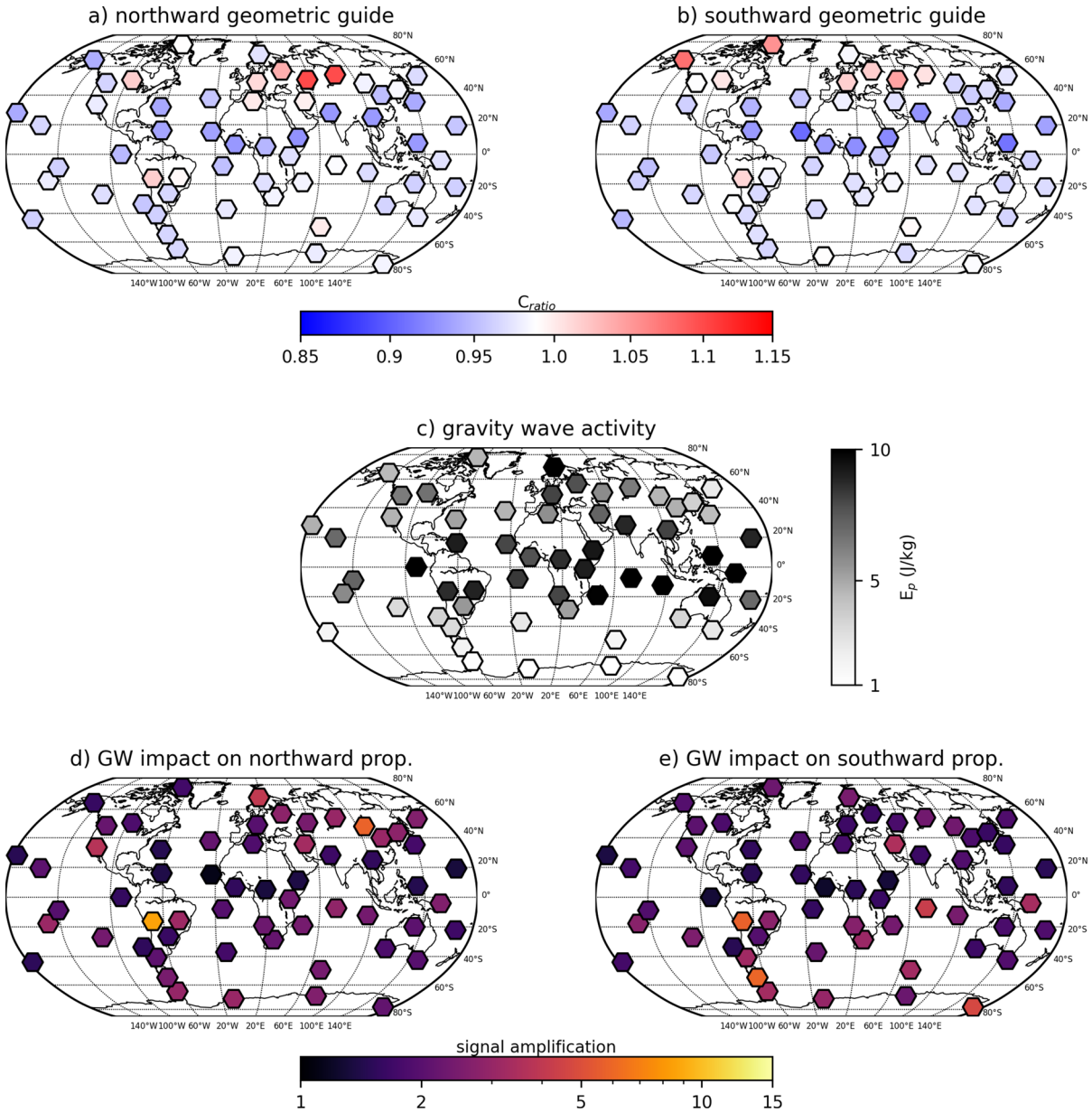

Figure 24
As Fig. 16 but for northward (315°–45°) and southward (135°–225°) propagation, using ICON-nwp outputs

References

Alexander, M. J., Beres, J. H., & Pfister, L. (2000). Tropical stratospheric gravity wave activity and relationships to clouds. *Journal of Geophysical Research: Atmospheres, 105*(D17), 22299–22309. https://doi.org/10.1029/2000JD900326

Baumgarten, G. (2010). Doppler Rayleigh/Mie/Raman lidar for wind and temperature measurements in the middle atmosphere up to 80 km. *Atmospheric Measurement Techniques, 3*, 1509–1518. https://doi.org/10.5194/amt-3-1509-2010

Baumgarten, G., Fiedler, J., Hildebrand, J., & Lübken, F.-J. (2015). Inertia gravity wave in the stratosphere and mesosphere observed by Doppler wind and temperature lidar. *Geophysical Research Letters, 42*, 10929–10936. https://doi.org/10.1002/2015GL066991

Blanc, et al. (2019). Middle atmosphere variability and model uncertainties as investigated in the framework of the ARISE project. *Infrasound Monitoring for Atmospheric Studies: Challenges in Middle Atmosphere Dynamics and Societal Benefits*. https://doi.org/10.1007/978-3-319-75140-5_28

Blom, P., & Waxler, R. (2021). Characteristics of thermospheric infrasound predicted using ray tracing and weakly non-linear waveform analyses. *The Journal of the Acoustical Society of America, 149*(5), 3174–3188. https://doi.org/10.1121/10.0004949

Bölöni, G., Kim, Y. H., Borchert, S., & Achatz, U. (2021). Toward transient subgrid-scale gravity wave representation in atmospheric models. Part I: Propagation model including nondissipative wave–mean-flow interactions. *Journal of the Atmospheric Sciences, 78*(4), 1317–1338. https://doi.org/10.1175/JAS-D-20-0065.1

Borchert, S., Zhou, G., Baldauf, M., Schmidt, H., Zängl, G., & Reinert, D. (2019). The upper-atmosphere extension of the ICON general circulation model (version: ua-icon-1.0). *Geoscientific Model Development, 12*(8), 3541–3569. https://doi.org/10.5194/gmd-12-3541-2019,2019

Brachet, N., Brown, D., Le Bras, R., Cansi, Y., Mialle, P., & Coyne, J. (2010). Monitoring the earth's atmosphere with the global IMS infrasound network. In A. Le Pichon, E. Blanc, & A. Hauchecorne (Eds.), *Infrasound Monitoring for Atmospheric Studies*. Dordrecht: Springer. https://doi.org/10.1007/978-1-4020-9508-5_3

Ceranna, L., Le Pichon, A., Green, D. N., & Mialle, P. (2009). The Buncefield explosion: A benchmark for infrasound analysis across Central Europe. *Geophysical Journal International, 177*(2), 491–508. https://doi.org/10.1111/j.1365-246X.2008.03998.x

Chunchuzov, I., & Kulichkov, S. (2019). Internal gravity wave perturbations and their impacts on infrasound propagation in the atmosphere. In A. Le Pichon, E. Blanc, & A. Hauchecorne (Eds.), *Infrasound Monitoring for Atmospheric Studies* (pp. 551–590). Cham: Springer.

Cugnet, D., de la Camara, A., Lott, F., Millet, C., Ribstein, B. (2019). Non-orographic gravity waves: representation in climate models and effects on infrasound. In: Le Pichon, A., Blanc, E., Hauchecorne, A. (eds) *Infrasound monitoring for atmospheric studies*. Cham: Springer. https://doi.org/10.1007/978-3-319-75140-5_27

De la Cámara, A., Lott, F., & Hertzog, A. (2014). Intermittency in a stochastic parameterization of nonorographic gravity waves. *Journal of Geophysical Research: Atmospheres, 119*(21), 11–905. https://doi.org/10.1002/2014JD022002

Drob, D. P., Broutman, D., Hedlin, M. A., Winslow, N. W., & Gibson, R. G. (2013). A method for specifying atmospheric gravity wavefields for long-range infrasound propagation calculations. *Journal of Geophysical Research: Atmospheres, 118*, 3933–3943. https://doi.org/10.1029/2012JD018077

Drob, D. P., Picone, J. M., & Garcés, M. (2003). Global morphology of infrasound propagation. *Journal of Geophysical Research, 108*(4680), D21. https://doi.org/10.1029/2002JD003307

Eichinger, R., Rhode, S., Garny, H., Preusse, P., Pisoft, P., Kuchař, A., Jöckel, P., Kerkweg, A., & Kern, B. (2023). Emulating lateral gravity wave propagation in a global chemistry–climate model (EMAC v2.55.2) through horizontal flux redistribution. *Geoscientific Model Development, 16*, 5561–5583. https://doi.org/10.5194/gmd-16-5561-2023

Ern, M., Trinh, Q. T., Preusse, P., Gille, J. C., Mlynczak, M. G., Russell, J. M., III., & Riese, M. (2017). GRACILE: A comprehensive climatology of atmospheric gravity wave parameters based on satellite limb soundings, link to data in NetCDF format. PANGAEA, doi: 10.1594/PANGAEA.879658 Supplement to: Ern, M et al. (2018): GRACILE: a comprehensive climatology of atmospheric gravity wave parameters based on satellite limb soundings. *Earth System Science Data, 10*(2), 857–892. https://doi.org/10.5194/essd-10-857-2018

Ern, M., Trinh, Q. T., Preusse, P., Gille, J. C., Mlynczak, M. G., Russell, J. M., III., & Riese, M. (2018). GRACILE: A comprehensive climatology of atmospheric gravity wave parameters based on satellite limb soundings. *Earth System Science Data, 10*, 857–892. https://doi.org/10.5194/essd-10-857-2018

Farges, T., Hupe, P., Le Pichon, A., Ceranna, L., Listowski, C., & Diawara, A. (2021). Infrasound thunder detections across 15 years over ivory coast: localization, propagation, and link with the stratospheric semi-annual oscillation. *Atmosphere, 12*(9), 1188. https://doi.org/10.3390/atmos12091188

Fritts, D. C., & Alexander, M. J. (2003). Gravity wave dynamics and effects in the middle atmosphere. *Reviews of Geophysics, 41*, 1003. https://doi.org/10.1029/2001RG000106

Gardner, C. S., Hostetler, C. A., & Franke, S. J. (1993). Gravity wave models for the horizontal wave number spectra of atmospheric velocity and density fluctuations. *Journal of Geophysical Research, 98*, 1035–1049. https://doi.org/10.1029/92JD02051

Green, D. N., Vergoz, J., Gibson, R., Le Pichon, A., & Ceranna, L. (2011). Infrasound radiated by the Gerdec and Chelopechene explosions: Propagation along unexpected paths. *Geophysical Journal International, 185*(2), 890–910. https://doi.org/10.1111/j.1365-246X.2011.04975.x

Hauchecorne, A., & Chanin, M. L. (1980). Density and temperature profiles obtained by lidar between 35 and 70 km. *Geophysical Research Letters, 7*(8), 565–568. https://doi.org/10.1029/GL007i008p00565

Hauchecorne, A., Chanin, M. L., Keckhut, P., et al. (1992). LIDAR monitoring of the temperature in the middle and lower atmosphere. *Applied Physics B, 55*, 29–34. https://doi.org/10.1007/BF00348609

Hedlin, M. A. H., & Drob, D. P. (2014). Statistical characterization of atmospheric gravity waves by seismoacoustic observations. *Journal of Geophysical Research: Atmospheres, 119*, 5345–5363.

Hertzog, A., Alexander, M. J., & Plougonven, R. (2012). On the intermittency of gravity wave momentum flux in the stratosphere. *Journal of Atmospheric Science, 69*, 3433–3448. https://doi.org/10.1175/JAS-D-12-09.1

Hohenegger, C., Korn, P., Linardakis, L., Redler, R., Schnur, R., Adamidis, P., Bao, J., Bastin, S., Behravesh, M., Bergemann, M., Biercamp, J., Bockelmann, H., Brokopf, R., Brüggemann, N., Casaroli, L., Chegini, F., Datseris, G., Esch, M., George, G., … Stevens, B. (2023). ICON-Sapphire: Simulating the components of the Earth system and their interactions at kilometer and subkilometer scales. *Geoscientific Model Development Discussions, 16*, 779–811. https://doi.org/10.5194/gmd-16-779-2023

Holton, J. R., & Hakim, G. J. (2013). *An introduction to dynamic meteorology* (5th ed.). Amsterdam: Elsevier Academic Press. https://doi.org/10.1016/C2009-0-63394-8

Keckhut, et al. (1993). A critical review of the database acquired for the long-term surveillance of the middle atmosphere by the French Rayleigh lidars. *Journal of Atmospheric and Oceanic Technology, 10*(6), 850–867. https://doi.org/10.1175/1520-0426(1993)010%3c0850:ACROTD%3e2.0.CO;2

Khaykin, et al. (2020). Doppler lidar at Observatoire de Haute-Provence for wind profiling up to 75 km altitude: Performance evaluation and observations. *Atmospheric Measurement Techniques, 13*(3), 1501–1516.

Kim, Y. H., Bölöni, G., Borchert, S., Chun, H. Y., & Achatz, U. (2021). Toward transient subgrid-scale gravity wave representation in atmospheric models. Part II: Wave intermittency simulated with convective sources. *Journal of the Atmospheric Sciences, 78*(4), 1339–1357. https://doi.org/10.1175/JAS-D-20-0066.1

Klocke, D., Brueck, M., Hohenegger, C., et al. (2017). Rediscovery of the doldrums in storm-resolving simulations over the tropical Atlantic. *Nature Geoscience, 10*, 891–896. https://doi.org/10.1038/s41561-017-0005-4

Köhler, L., Green, B., & Stephan, C. C. (2023). Comparing loon superpressure balloon observations of gravity waves in the tropics with global storm-resolving models. *Journal of Geophysical Research: Atmospheres, 128*(15), e2023JD038549. https://doi.org/10.1029/2023JD038549

Le Pichon, A., Ceranna, L., & Vergoz, J. (2012). Incorporating numerical modeling into estimates of the detection capability of the IMS infrasound network. *Journal of Geophysical Research, 117*, D05121. https://doi.org/10.1029/2011JD016670

Le Pichon, A., Ceranna, L., Vergoz, J., & Tailpied, D. (2019). Modeling the detection capability of the global IMS infrasound network. *Infrasound Monitoring for Atmospheric Studies* (pp. 593–604). Cham: Springer.

Listowski, C., Forestier, E., Dafis, S., Farges, T., De Carlo, M., Grimaldi, F., Le Pichon, A., Vergoz, J., Heinrich, P., & Claud, C. (2022). Remote monitoring of mediterranean hurricanes using infrasound. *Remote Sensing, 14*, 6162. https://doi.org/10.3390/rs14236162

Marchetti, E., Ripepe, M., Campus, P., et al. (2019). Long range infrasound monitoring of Etna volcano. *Science and Reports, 9*, 18015. https://doi.org/10.1038/s41598-019-54468-5

Mzé, N., Hauchecorne, A., Keckhut, P., & Thétis, M. (2014). Vertical distribution of gravity wave potential energy from long-term Rayleigh lidar data at a northern middle-latitude site. *Journal of Geophysical Research: Atmospheres, 119*(21), 12–069. https://doi.org/10.1002/2014JD022035

Pierce, A. D. (2019). *Acoustics: An introduction to its physical principles and applications*. Springer.

Pilger, C., Gaebler, P., Hupe, P., et al. (2021). Yield estimation of the 2020 Beirut explosion using open access waveform and remote sensing data. *Science and Reports, 11*, 14144. https://doi.org/10.1038/s41598-021-93690-y

Pilger, C., Gaebler, P., Hupe, P., Ott, T., & Drolshagen, E. (2020). Global monitoring and characterization of infrasound signatures by large fireballs. *Atmosphere, 11*(1), 83. https://doi.org/10.3390/atmos11010083

Pilger, C., Hupe, P., & Koch, K. (2023). The state of the stratosphere throughout the seasons: How well can atmospheric models explain infrasound observations at regional distances? *Pure and Applied Geophysics, 180*, 1375–1393. https://doi.org/10.1007/s00024-022-03055-3

Plougonven, R., de la Cámara, A., Hertzog, A., & Lott, F. (2020). How does knowledge of atmospheric gravity waves guide their parameterizations? *Quarterly Journal of the Royal Meteorological Society, 146*(728), 1529–1543. https://doi.org/10.1002/qj.3732

Plougonven, R., & Zhang, F. (2014). Internal gravity waves from atmospheric jets and fronts. *Reviews of Geophysics, 52*(1), 33–76. https://doi.org/10.1002/2012RG000419

Polichtchouk, I., Van Niekerk, A., & Wedi, N. (2023). Resolved gravity waves in the extratropical stratosphere: Effect of horizontal resolution increase from O (10) to O (1) km. *Journal of the Atmospheric Sciences, 80*(2), 473–486. https://doi.org/10.1175/JAS-D-22-0138.1

Popov, O. E., Mishenin, A. A., Kulichkov, S. N., Chunchuzov, I. P., Perepelkin, V. G., & Ceranna, L. (2022). The effect of the stratopause on the structure of the infrasound signal from the August 4, 2020, Beirut explosion. *The Journal of the Acoustical Society of America, 152*(1), 99–106. https://doi.org/10.1121/10.0012191

Smith, S. A., Fritts, D. C., & Vanzandt, T. E. (1987). Evidence for a saturated spectrum of atmospheric gravity waves. *Journal of Atmospheric Sciences, 44*(10), 1404–1410. https://doi.org/10.1175/15200469(1987)044%3c1404:EFASSO%3e2.0.CO;2

Stephan, C. C., Duras, J., Harris, L., Klocke, D., Putman, W. M., Taylor, M., Wedi, N. P., Žagar, N., & Ziemen, F. (2022). Atmospheric energy spectra in global kilometre-scale models. *Tellus A: Dynamic Meteorology and Oceanography, 74*(1), 280–299. https://doi.org/10.16993/tellusa.26

Stephan, C. C., Schmidt, H., Zülicke, C., & Matthias, V. (2020). Oblique gravity wave propagation during sudden stratospheric warmings. *Journal of Geophysical Research: Atmospheres, 125*(1), e2019JD031528. https://doi.org/10.1029/2019JD031528

Stephan, C. C., Strube, C., Klocke, D., Ern, M., Hoffmann, L., Preusse, P., & Schmidt, H. (2019a). Intercomparison of gravity waves in global convection-permitting models. *Journal of the Atmospheric Sciences, 76*(9), 2739–2759. https://doi.org/10.1175/JAS-D-19-0040.1

Stephan, C. C., Strube, C., Klocke, D., Ern, M., Hoffmann, L., Preusse, P., & Schmidt, H. (2019b). Gravity waves in global high-resolution simulations with explicit and parameterized convection. *Journal of Geophysical Research: Atmospheres, 124*, 4446–4459. https://doi.org/10.1029/2018JD030073

Stevens, B., Satoh, M., Auger, L., et al. (2019). DYAMOND: The dynamics of the atmospheric general circulation modeled on non-hydrostatic domains. *Progress in Earth and Planetary Science, 6*, 61. https://doi.org/10.1186/s40645-019-0304-z

Sutherland, L. C., & Bass, H. E. (2004). Atmospheric absorption in the atmosphere up to 160 km. *Journal of the Acoustical Society of America, 115*, 1012–1032. https://doi.org/10.1121/1.1631937

Vallage, A., et al. (2021). Multitechnology characterization of an unusual surface rupturing intraplate earthquake: The ML 5.4 2019 Le Teil event in France. *Geophysical Journal International, 226*(2), 803–813. https://doi.org/10.1093/gji/ggab136

Vorobeva, E., Assink, J., Espy, P. J., Renkwitz, T., Chunchuzov, I., & Näsholm, S. P. (2023). Probing gravity waves in the middle atmosphere using infrasound from explosions. *Journal of Geophysical Research: Atmospheres, 128*(13), e2023JD038725. https://doi.org/10.1029/2023JD038725

Waxler, R., & Assink, J. (2019). Propagation modeling through realistic atmosphere and benchmarking. *Infrasound monitoring for atmospheric studies: Challenges in middle atmosphere dynamics and societal benefits*. https://doi.org/10.1007/978-3-319-75140-5

Waxler, R., Hetzer, C., Assink, J., Velea, D. (2021). chetzer-ncpa/ncpaprop-release: NCPAprop v2.1.0 (v2.1.0). Zenodo. https://doi.org/10.5281/zenodo.5562713

Wing, R., et al. (2021). Intercomparison and evaluation of ground- and satellite-based stratospheric ozone and temperature profiles above Observatoire de Haute-Provence during the Lidar validation NDACC Experiment (LAVANDE. *Atmospheric Measurement Techniques, 13*, 5621–5642. https://doi.org/10.5194/amt-13-5621-2020

Zängl, G., Reinert, D., Ripodas, P., & Baldauf, M. (2015). The ICON (icosahedral non-hydrostatic) modelling framework of DWD and MPIM: Description of the non-hydrostatic dynamical core. *Quarterly Journal of the Royal Meteorological Society, 141*, 563–579. https://doi.org/10.1002/qj.2378

(Received November 15, 2023, revised March 11, 2024, accepted March 12, 2024)